Chemical Engineering Journal 451 (2023) 138624

Contents lists available at ScienceDirect

Chemical Engineering Journal

journal homepage: www.elsevier.com/locate/cej

In-situ-construction of BiOI/UiO-66 heterostructure via nanoplate-on-octahedron: A novel p-n heterojunction photocatalyst for efficient sulfadiazine elimination

Tianyu Wang [a], Chen Zhao [a,*], Linghui Meng [a], Yujia Li [a], Hongyu Chu [a], Fei Wang [a], Yingru Tao [a], Wen Liu [b], Chong-Chen Wang [a,*]

[a] *Beijing Key Laboratory of Functional Materials for Building Structure and Environment Remediation, Beijing University of Civil Engineering and Architecture, Beijing 100044, China*

[b] *College of Environmental Sciences and Engineering, Peking University, Key Laboratory of Water and Sediment Sciences, Ministry of Education, Beijing 100871, China*

ARTICLE INFO

Keywords:
UiO-66
BiOI
p-n heterojunction
Photocatalysis
Antibiotic removal

ABSTRACT

Sulfadiazine (SDZ), as a broad-spectrum pharmaceutical antibiotic, has drawn extensive attention owing to its wide application and persistence. Photocatalytic oxidation has been considered as a high-efficiency and environment-friendly technology for degrading organic contaminants. A novel BiOI/UiO-66 p-n heterojunction (BiU-*x*) was fabricated via the *in-situ* deposition of p-type BiOI nanoplates on n-type UiO-66 octahedrons with the aid of a controlled precipitation method. The optimizing BiU-9 heterojunction exhibited a remarkably enhanced photocatalytic efficiency in removing SDZ, in which the SDZ (5 mg/L) removal efficiency over BiU-9 (0.5 g/L) reached nearly 100 % within 90 min of visible light irradiation. The influence of some important environmental factors (e.g., photocatalyst dosage, pH, co-existing inorganic anions and real sunlight irradiation) were systematically investigated. Such improvement mechanism should be assigned to the following three factors. Firstly, the introduction of narrow gap semiconductor BiOI effectively improved photo adsorption capacity. Secondly, benefiting by the large specific surface area, the involvement of UiO-66 contributed to boost the surface active sites. Most importantly, an internal electric field at the contact interface between UiO-66 and BiOI accelerated the separation of photo-generated electrons and holes. Furthermore, $\cdot O_2^-$ and photo-generated holes were identified as the dominating reactive species accounting for the SDZ removal. The decomposition pathways of SDZ and ecotoxicities of the intermediates were analyzed via combing with LC-MS/MS and T.E.S.T theoretical calculation. This work may provide an alternative way for enhanced photocatalytic performance of MOF-based materials through construction of p-n heterojunction with bismuth-based semiconductors.

1. Introduction

Sulfadiazine (SDZ, $C_{10}H_{10}N_4O_2S$) is one of the synthetic sulfanilamide antibiotics, has been diffusely utilized in the treatment of human diseases and animal feeding. In China, approximately 1260 tons of SDZ can be consumed every year, making it the second largest used antibiotic in commonly used sulfanilamide antibiotics [1]. Owing to its long persistence and high mobility, SDZ has been frequently found in various aquatic environments, such as surface waters [2], industrial effluents [3] and wastewater treatment plants (WWTPs) [4]. Therefore, the abuse of SDZ and its long-term exposure property will inevitably cause potential ecological risk. Considering that SDZ possesses low biodegradability and high stability [5], it cannot be efficiently eliminated by traditional water treatment technologies, such as adsorption and biological technologies [6–8]. The adsorption-based technologies benefit the advantages like simplicity of design and ease of operation. However, secondary contamination from adsorbents strongly limits its development and applications [9]. Escher and co-workers [10] suggested that only 60 % of toxic pharmaceuticals could be removed during the biological treatment processes. In addition, the efficiency of traditional biological treatments in removing sulfonamides is markedly dependent on seasonal variations [11]. As a result, a novel technology to effectively treat SDZ-containing wastewaters is urgently anticipated.

The feasibility of advanced oxidation processes (AOPs) to remove

* Corresponding authors.
E-mail addresses: zhaochen1@bucea.edu.cn (C. Zhao), wangchongchen@bucea.edu.cn (C.-C. Wang).

https://doi.org/10.1016/j.cej.2022.138624

Available online 13 August 2022

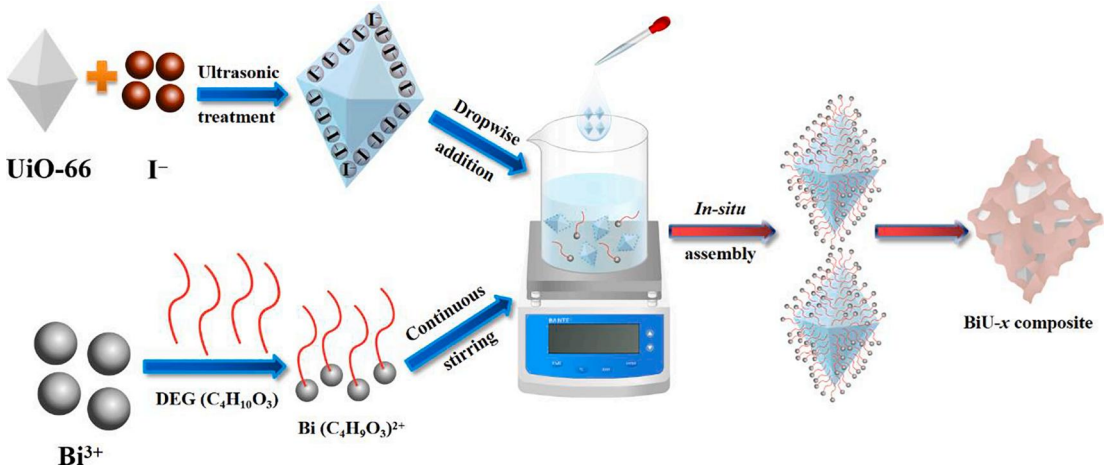

Scheme 1. Schematic illustration of *in-situ* precipitation route for preparing BiU-*x* heterojunctions.

sulfonamide antibiotics in wastewaters has been widely demonstrated [12,13]. The heterogeneous photocatalysis, belonging to the AOPs, is an environmentally friendly option for eliminating persistent organic pollutants [14]. Owing to its merits of remarkable efficiency, mild reaction conditions and long-term stability, photocatalytic oxidation technology can directly utilize real sunlight as reaction energy to drive the decomposition and eventual mineralization of organic pollutants. Thus, it has gradually become an appealing strategy for dealing with different environmental issues [15,16]. However, the kernel of photocatalysis is the development of new photocatalysts with excellent sunlight harvesting and sufficient separation efficiency of photo-generated charge carriers. Within them, bismuth oxyhalides (BiOX, X = Cl, Br, I) show huge potential in photocatalytic purification of organic contaminants under the illumination of visible light by virtue of unique electronic band structure, low toxicity, controlled morphology and reasonable chemical stability [17]. Among BiOX photocatalysts, BiOI is a p-type semiconducting material with layered crystal configuration. The narrow band gap of BiOI (1.72–1.94 eV) enables it to possess impressive photocatalytic performances for organic contaminants decomposition under both UV and visible light irradiation [18]. However, BiOI with 2D lamellar structure is liable to agglomerate, resulting in restricted active sites limited its adsorption capacity for target pollutants [19]. Furthermore, pristine BiOI has high recombination rate of charge carriers, which severely limits the generation of active species during photocatalytic process [20]. Therefore, it is of significant interest to develop an outstanding BiOI-based photocatalyst with improved photocatalytic performance for purifying SDZ-containing wastewater.

Currently, the fabrication of p-n heterojunction has been perceived as an ideal methods to suppress the recombination of photo-generated carriers due to the presence of a powerful internal electric field (IEF) at the interface of p-n heterojunction, which is beneficial to efficiently facilitate the separation of charge carriers with the aid of opposite migration of photo-generated electrons and holes, resulting in the prominent improvement of photocatalytic activity [21,22]. For example, some BiOI-based p-n heterojunctions have been constructed consequently, such as $BiPW_{12}O_{40}$/BiOI [23], $BiPO_4$/BiOI [24], BiOI/ZnO [25] and g-C_3N_4/BiOI [26]. The above binary photocatalysts have successfully achieved the spatial separation of photo-generated electron-hole pairs.

Unlike traditional semiconductor photocatalysts, metal–organic frameworks (MOFs) are periodic crystalline structures consisted by self-assembly of organic ligands and metal ions [27]. Benefiting from the merits of large specific surface area [28], adjustable structure and semiconductor property, MOFs can be directly used as photocatalysts or acted as the carriers for supporting bismuth-based photocatalysts. For one thing, this can enhance the transfer of photo-generated charge carriers. For another, it is feasible to regulate the growth of bismuth-based semiconductors on the surface of MOFs and reduce their agglomeration, thereby exposing more active sites. In 2021, our research group summarized the photocatalytic applications of MOF/bismuth-based semiconductor composites (MBCs) [16], we found that most of MBCs could be classified as I-scheme, II-scheme or Z-scheme heterojunctions and their applications for removal of antibiotics were still preliminary. As a consequence, it is indispensable to integrate the superiorities of BiOI and MOF into a p-n heterojunction photocatalyst to efficient removal of SDZ antibiotic.

Among the different types of MOFs, Zr-based MOFs possess stronger chemical and thermal stability. Particularly, UiO-66 ($Zr_{24}O_{120}C_{192}H_{96}$) is a star Zr-based MOF and has been diffusely applied in the field of photocatalytic reactions [29]. More importantly, UiO-66 shows good structural stability in water environments and typical n-type property [30]. Enlightened by above facts, BiOI/UiO-66 p-n heterojunctions (BiU-*x*) with nanoplate-on-octahedral heterostructure were successfully fabricated via *in-situ* precipitation route. Integrating UiO-66 with BiOI was expected not only to effectively prevent the BiOI aggregation, but also to improve the photo-adsorption capacity and to inhibit the recombination of electron-hole pairs, resulting in the remarkable enhancement of the photocatalytic degradation of SDZ under visible light and real sunlight through the synergistic effect. Various factors were systematically explored, such as photocatalyst dosage, pH and co-existing inorganic anions. Moreover, the photocatalytic degradation pathways and reaction mechanism were investigated based on LC-MS/MS analysis, photo-electro-chemistry characterization, energy band alignment and active species determination. Additionally, the ecotoxicities of degradation intermediates were analyzed by T.E.S.T. tool on the basis of quantitative structure–activity relationship.

2. Experimental

2.1. Materials and reagents

Anhydrous Zirconium (IV) chloride ($ZrCl_4$, 98 %, CAS: 10026-11-6), terephthalic acid (H_2BDC, 99 %, CAS: 100-21-0), tertbutyl alcohol (TBA, 99.5 %, CAS: 75-65-0), acetonitrile (99.8 %, CAS: 75-05-8) and sulfadiazine (SDZ, 99 %, CAS: 68-35-9) were purchased from J&K Scientific Technology Company. Diethylene glycol (DG, 98 %, CAS: 111-46-6), potassium iodide (KI, 99 %, CAS: 7681-11-0), L-histidine (99 %, CAS: 71-00-1) and phosphoric acid (PA, 85 %–90 %, CAS: 7664-38-2) were obtained from Shanghai Macklin Biochemical Company. *N,N'*-dimethylformamide (DMF, 98 %, CAS: 68-12-2), acetic acid (HAC, 98 %, CAS: 64-19-7), ethanol (EtOH, 99 %, CAS: 64-17-5), hydrochloric acid (HCl, 37 %, CAS: 7647-01-0), sodium hydroxide (NaOH, 97 %, CAS: 1310-73-

2) and triethanolamine (TEA, 99 %, CAS: 102-71-6) were purchased from Tianjin Fu Chen Chemical Reagents Factory. Bismuth nitrate pentahydrate ($Bi(NO_3)_3{\cdot}5H_2O$, 99.9 %, CAS: 10035-06-0) was obtained from Shanghai Aladdin Bio-Chem Technology Company. *p*-Benzoquinone (BQ, 99 %, CAS: 106-51-4) were purchased from Tianjin Guang Fu Fine Chemical Research Institute.

2.2. Photocatalysts preparation

2.2.1. Synthesis of UiO-66

UiO-66 was synthesized through solvothermal method according to the reported study with slightly modification [31]. Typically, $ZrCl_4$ (40 mg, 0.1716 mmol) and H_2BDC (28.5 mg, 0.1716 mmol) were dispersed in 5 mL DMF, respectively. Then HAC (3.0 mL) was introduced into the former suspension, and the obtained mixture was encapsulated in a Teflon-lined autoclave with a volume of 25 mL and heated at 120 °C for 24 h. After that, the white precipitates were rinsed with DMF for three times and obtained via centrifugation process. Eventually, the white UiO-66 powders were dried in an oven at 60 °C overnight for follow-up applications.

2.2.2. Fabrication of BiU-*x* heterojunctions

The BiU-*x* heterojunctions were fabricated via a mild diethyleneglycol-assisted *in-situ* precipitation method at room temperature, as schematically illustrated in Scheme 1. Typically, 485 mg $Bi(NO_3)_3{\cdot}5H_2O$ was dispersed into 20 mL DG to get a uniform solution A. Then, different amounts of UiO-66 octahedrons (10 %, 30 %, 50 %, 70 %, 90 % and 110 % to the weight of stoichiometric prepared BiOI, respectively) were added into 8.3 g/L KI solution, and the solution B was obtained via the continuous stirring for 60 min. Subsequently, the solution B was dropwise added into the solution A and the formed isotropical solution was kept stirring for 180 min. The solid samples were withdrawn by centrifugation with ethanol and ultrapure water for least three times. After drying in a vacuum oven at 80 °C for 12 h, the BiU-*x* heterojunctions were finally collected. BiU-*x* with UiO-66:BiOI mass percentages of 10 %, 30 %, 50 %, 70 %, 90 % and 110 % were named as BiU-1, BiU-3, BiU-5, BiU-7, BiU-9 and BiU-11, respectively. The pristine BiOI was synthesized by the similar procedure except for adding UiO-66 octahedrons.

Besides, the details of the electrochemical measurements including photocurrent density, Mott-Schottky curves and EIS (electrochemical impedance spectra) were shown in Electronic Supplementary Information (ESI).

2.3. Characterizations

The powder X-ray diffraction (PXRD) patterns were examined on a DX-2700B X-ray diffractometer. The Cu K_α line was used as the radiation source. Fourier transform infrared spectra (FT-IR) were collected on a Nicolet 6700 infrared spectrophotometer. The UV–vis diffuse reflectance spectra (UV–vis DRS) were measured by a PerkinElmer Lambda 650S spectrophotometer with $BaSO_4$ as the reference. The morphologies were determined by a Hitachi SU8020 scanning electron microscopy (SEM), JEM 1200EX transmission electron microscopy (TEM) and Tecnai G2 F20 high resolution transmission electron microscope (HRTEM). The X-ray photoelectron spectra (XPS) and valence band X-ray photoelectron spectra (VB-XPS) were acquired by a ThermoFisher Escalab 250XI electron spectrometer with Al K_α radiations. The Brunauer-Emmett-Teller (BET) surface area and N_2 adsorption–desorption isotherm were obtained by a Micromeritics ASAP 2460 physical adsorption instrument. The photoluminescence (PL) spectra were detected by a Hitachi F-7000 fluorescence spectrophotometer.

2.4. Photocatalytic test

The photocatalytic efficiencies of the UiO-66, BiOI and BiU-*x* were assessed by the decomposition of SDZ aqueous solution under visible light and real sunlight illumination. A multitube photocatalytic reactor (PCX50C, Beijing Perfectlight Technology Company) was used to carry out photocatalytic experiments, its appearance and structure were shown in Figure S1. A 5 W LED lamp worked as the illumination source. The initial pH of SDZ solution was regulated by NaOH or HCl. For each experiment, a certain amount of photocatalyst was added into 50 mL of SDZ aqueous solution (5 mg/L) under magnetic stirring. Before photocatalysis process, an adsorption–desorption equilibrium was obtained in a darkness circumstance. At a certain interval, 2.5 mL of the mixture was taken out and filtered via a 0.22 μm Nylon membrane for follow-up analysis. The concentration of SDZ was monitored by a Vanquish Duo high performance liquid chromatograph (HPLC, Shimadzu) equipped with a C18 column (2.1 mm × 250 mm, 5.0 μm). The mobile phase consisted of acetonitrile/phosphoric acid (45/55, *v/v*) at a flow rate of 0.8 mL/min. The column temperature was maintained at 40 °C and the UV detection wavelength was set as 355 nm. The determination of the photodegradation products was performed by a Thermo Dionex UltiMate 3000 ultra-performance liquid chromatography equipped with a Thermo Scientific Q Exactive. Eclipse Plus C-18 chromatographic column (100 mm × 4.6 mm, 3.5 μm) was used to separate the different types of organic compounds. The mobile phase was consistent with HPLC analysis but the flow rate was set as 0.5 mL/min. The MS spectra were recorded over the range of 50–600 *m/z*. The photocatalytic efficiency was calculated by the Eq. (1):

$$\text{Degradation}\ (\%) = (1 - C_t/C_0) \times 100\ \% \quad (1)$$

where C_0 and C_t denoted the SDZ concentrations in the initial and photodegraded samples at given sampling intervals, respectively.

Table 1
The levels and ranges of variables in Box–Behnken statistical experiment design.

Independent variables	Symbol	Coded variable level		
		Low (−1)	Center (0)	High (+1)
Cl^-, mg/L	A	0	1400	2800
SO_4^{2-}, mg/L	B	0	80	160
NO_3^-, mg/L	C	0	3.55	7.1
HCO_3^-, mg/L	D	0	11	22

2.5. Design and analysis of co-existing inorganic anions

To evaluate the influences of co-existing inorganic anions on the SDZ removal more scientifically, response surface methodology (RSM) was used to design experiments and assess the interaction effect of the inorganic anions [32].

2.5.1. Experimental design of Box-Behnken

The experimental design of Box-Behnken was used to evaluate the effect of four operating parameters more accurately and systematically, i.e., Cl^- (mg/L), SO_4^{2-} (mg/L), NO_3^- (mg/L) and HCO_3^- (mg/L), which were labeled as A, B, C and D, respectively. The above chosen parameters were deemed as the independent variables and the degradation efficiency (%) after photocatalytic process was selected as the dependent variable (response). The concentration ranges of four inorganic anions were based on the previous reports [33,34], as illustrated in Table 1. In view of the above, 29 sets of experiments were defined for these four independent variables at three levels (coded as −1, 0, +1).

2.5.2. RSM model

With respect to RSM, a second-order polynomial equation (Eq. (2)) was acquired to model the photodegradation efficiency as a function of the above mentioned independent variables.

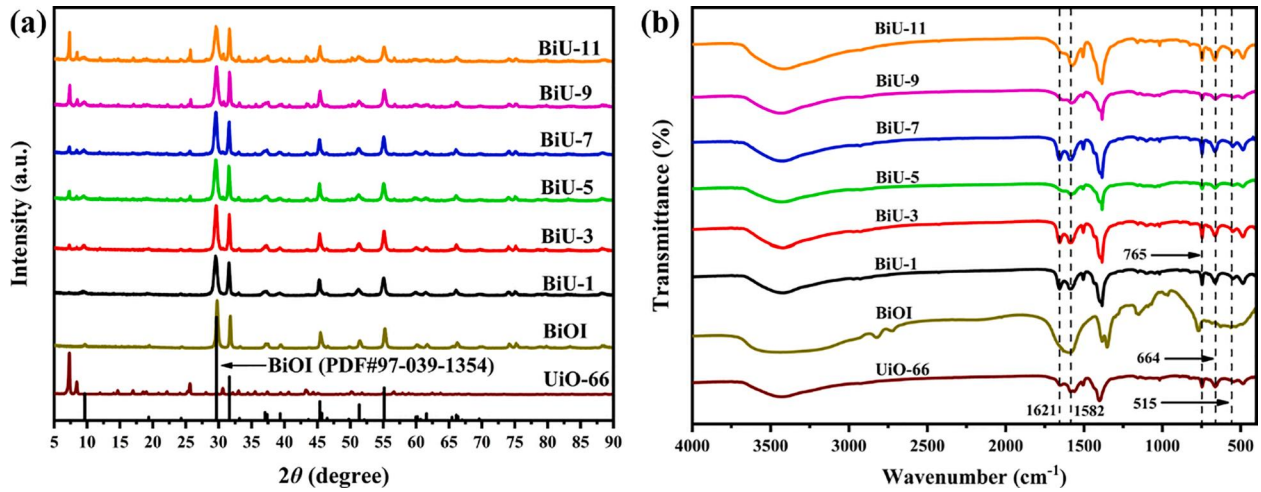

Fig. 1. (a) PXRD patterns and (b) FT-IR spectra of the BiOI, UiO-66 and BiU-*x* samples.

$$Y = \beta_0 + \beta_1 A + \beta_2 B + \beta_3 C + \beta_4 D + \beta_{12} AB + \beta_{13} AC + \beta_{14} AD + \beta_{23} BC + \beta_{24} BD + \beta_{34} CD + \beta_{11} A^2 + \beta_{22} B^2 + \beta_{33} C^2 + \beta_{44} D^2 \quad (2)$$

where Y is the degradation efficiency (%) (response), β_0 represents the interception coefficient, β_1, β_2, β_3, and β_4 are the coefficients of the independent variables, β_{11}, β_{22}, β_{33}, and β_{44} are the quadratic terms, and β_{12}, β_{13}, β_{14}, β_{23}, β_{24}, and β_{34} are the interaction coefficients [35]. Furthermore, we used Design-Expert® software (Minneapolis, USA) to accomplish the analysis of variance (ANOVA) and optimization of photocatalytic efficiency.

2.6. Identification of reactive species

To ascertain the contributory roles of the generated reactive species during photocatalytic process, the sacrificial agents such as TBA (50 mmol/L), *p*-BQ (1 mmol/L), L-histidine (1 mmol/L) and TEA (50 mmol/L) were separately added in SDZ aqueous solution to capture hydroxyl radicals (·OH), superoxide radicals ($\cdot O_2^-$), singlet oxygen ($^1O_2$) and photo-generated holes (h^+). The electronic spin resonance (ESR) measurements were carried out using a Bruker A300-10/12 Electron paramagnetic resonance spectrometer to verify the generation of ·OH and $\cdot O_2^-$ during photocatalytic process. Generally, 10 mg of photocatalyst

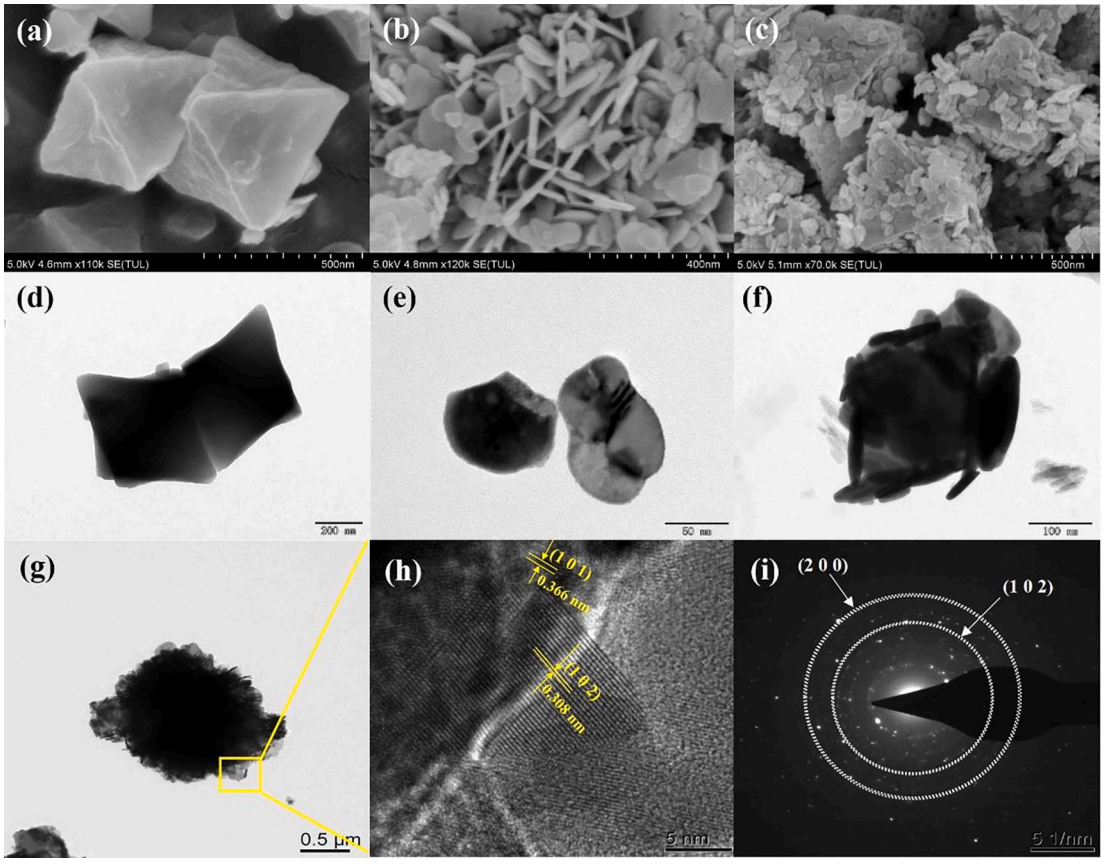

Fig. 2. SEM and TEM micrographs of (a, d) UiO-66, (b, e) BiOI, (c,f) BiU-*x* heterojunction photocatalyst; (g)-(i) HRTEM micrographs and SAED pattern of the selected BiU-*x* heterojunction photocatalyst.

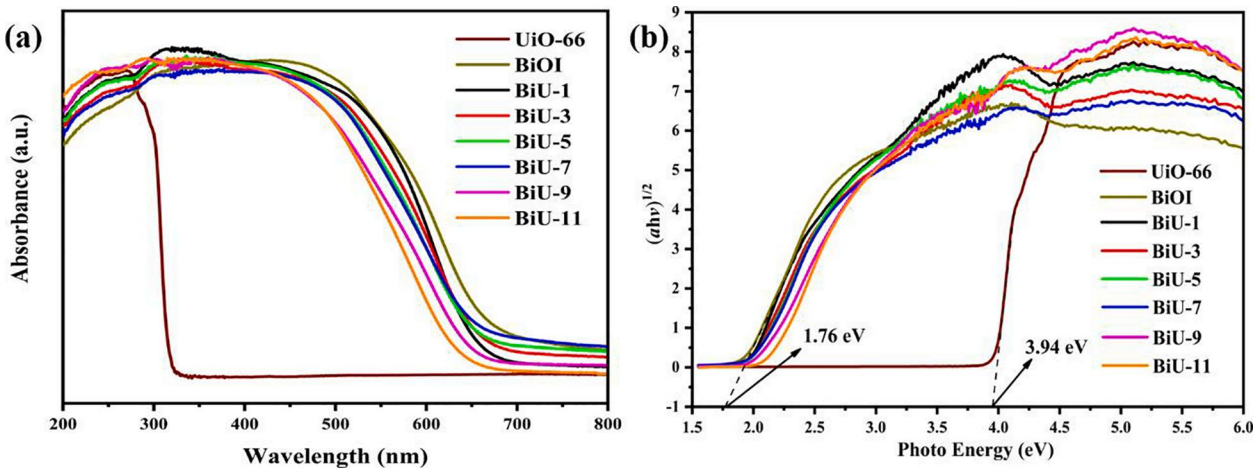

Fig. 3. (a) UV–vis DRS spectra and (b) the E_g plots of BiOI, UiO-66 and BiU-*x* heterojunctions.

was dispersed in 5 mL methanol, then the signals of ·OH and $\cdot O_2^-$ can be captured by 5,5-dimethyl-1-pyrroline N-oxide (DMPO) and the adducts of DMPO-·OH and DMPO-$\cdot O_2^-$ will be detected by ESR technique.

2.7. Density functional theory (DFT) calculations

DFT calculation based on Fukui index was introduced to study the reactive sites of SDZ molecule under the attack of different active species. Considering that the free radicals produced by this reaction system were electrophilic, therefore Fukui index representing electrophilic (f^-) attack was analyzed [36]. These Fukui values were obtained from the Peking University Reactive Sites for Organic Compounds Database (PKU-REOD) [37], and the DFT calculations were accomplished by the Gaussian 16C.01 software. Natural population analysis (NPA) charge was used to evaluate the electron activity [38]. The geometrical optimization of molecule and vibrational frequencies calculations were conducted using the B3LYP method with 6–31+G(d,p) basis set.

3. Results and discussion

3.1. Characterization

3.1.1. PXRD and FT-IR spectra

PXRD was used to characterize the crystal structures of the prepared materials. As depicted in Fig. 1(a), the main diffraction peaks of pristine UiO-66 were in line with the results reported in our former reports [39,40], indicating that UiO-66 was successfully synthesized in this work. With regard to BiOI, the characteristic diffraction peaks centered at 9.6°, 29.6°, 31.6°, 45.4° and 55.1° were corresponded to the (001), (102), (110), (200) and (212) crystalline planes of tetragonal BiOI (JCPDS No. 73-2062). No presence of diffraction peaks from impurities suggested its high purity. Obviously, the PXRD patterns of BiU-*x* heterojunctions contained the whole of diffraction peaks of UiO-66 and BiOI, respectively, suggesting the co-existence of UiO-66 and BiOI in the as-prepared heterojunctions. More importantly, it can be found that the intensities of the (111) and (200) peaks from UiO-66 at 7.4° and 8.5° gradually strengthened in the patterns of BiU-*x* heterojunctions with the increasing of UiO-66 content, indicating that the precipitation of BiOI still preserved the crystal texture of UiO-66 framework.

The FT-IR spectra were used to confirm the chemical bonding and functional groups of pristine UiO-66, BiOI and BiU-*x* heterojunctions [41]. As illustrated in Fig. 1(b), the wide adsorption bands at 3200–3500 cm^{-1} were ascribed to the stretching vibration of O—H from absorbed H_2O molecules [42]. As for pristine BiOI, the adsorption peak at 515 cm^{-1} in the spectrum was assigned to symmetrical A_{2u}-type vibration of the Bi–O bond [43]. In the FTIR spectrum of UiO-66, the main peaks at 1582 cm^{-1} and 1621 cm^{-1} should be attributed to the C═O stretching modes and vibrations from benzene ring structures [44]. Another characteristic peaks ranging from 1400 to 1500 cm^{-1} verified the existence of C═C and C—C functional groups originated from the organic ligand in MOFs [45]. Moreover, the characteristic peaks located at 664 cm^{-1} and 765 cm^{-1} were associated with C—H and O—H vibration modes [46]. In addition, the main peaks ranging from 800 to 600 cm^{-1} were ascribed to O–Zr–O groups [47]. It was a remarkable fact that compared with the wider adsorption band of Bi–O (centered at 515 cm^{-1}) for pristine BiOI, the corresponding peaks became more intense in the BiU-*x* heterojunctions, which might be ascribed to the creation of close interfacial contact between UiO-66 and BiOI.

3.1.2. Morphology features

The external micro topographies and the microstructures of the representative samples were investigated by SEM, TEM and HRTEM. As depicted in Fig. 2(a) and (d), UiO-66 exhibited uniform and smooth octahedral structure with diameter about 500 nm. The pristine BiOI structure was composed of plenty of nanoplates with size of 50–200 nm (Fig. 2(b) and (e)). After combination, it could be clearly seen that the UiO-66 and BiOI was *in-situ* assembled together, the BiOI nanoplates were stacked on the surfaces of UiO-66 and relatively large UiO-66 octahedrons acted as an ideal platform for BiOI nanoplates to grow on. Furthermore, the morphological and structural features of BiU-*x* was analyzed by TEM and HRTEM (Fig. 2(g)-(i)). Importantly, the HRTEM image (Fig. 2(h)) exhibited the close interfacial contact between UiO-66 and BiOI, further proving the formation of heterostructure. Moreover, some lattice fringes were arranged regularly and can be detected in Fig. 2(h) suggested that the BiU-*x* sample possessed good crystallinity of BiOI. And the lattice fringes of 0.308 nm and 0.366 nm can be associated with the (102) and (101) planes of BiOI [48,49]. At the same time, a sequence of concentric rings in the SAED (Fig. 2(i)) should be assigned to the (102) and (200) planes of BiOI (JCPDS No. 73-2062) [50,51]. To further illustrated the distribution of BiOI on UiO-66, EDS-mapping was depicted in Fig. S2. The elements of Bi, Zr, I and O were clearly observed, and their distributions were homogenous.

Based on the SEM, TEM and HRTEM results, the generation process of BiU-*x* was proposed as illustrated in Scheme 1. Firstly, diethylene glycol can interact with Bi^{3+} to generate homogeneous alkoxides solution ($Bi(C_4H_9O_3)^{2+}$), which was beneficial to prevent the hydrolysis of Bi^{3+} cations and its high homogeneity level was conducive to combine with the other materials. Meanwhile, KI solution was fully dispersed with UiO-66 octahedrons, resulting in I^- anions surrounded around UiO-66. After the addition of solution B, $Bi(C_4H_9O_3)^{2+}$ will react with I^- to generate BiOI nanoplates. To keep low surface energy, these BiOI nanoplates were inclined to *in-situ* deposition on the surface of UiO-66

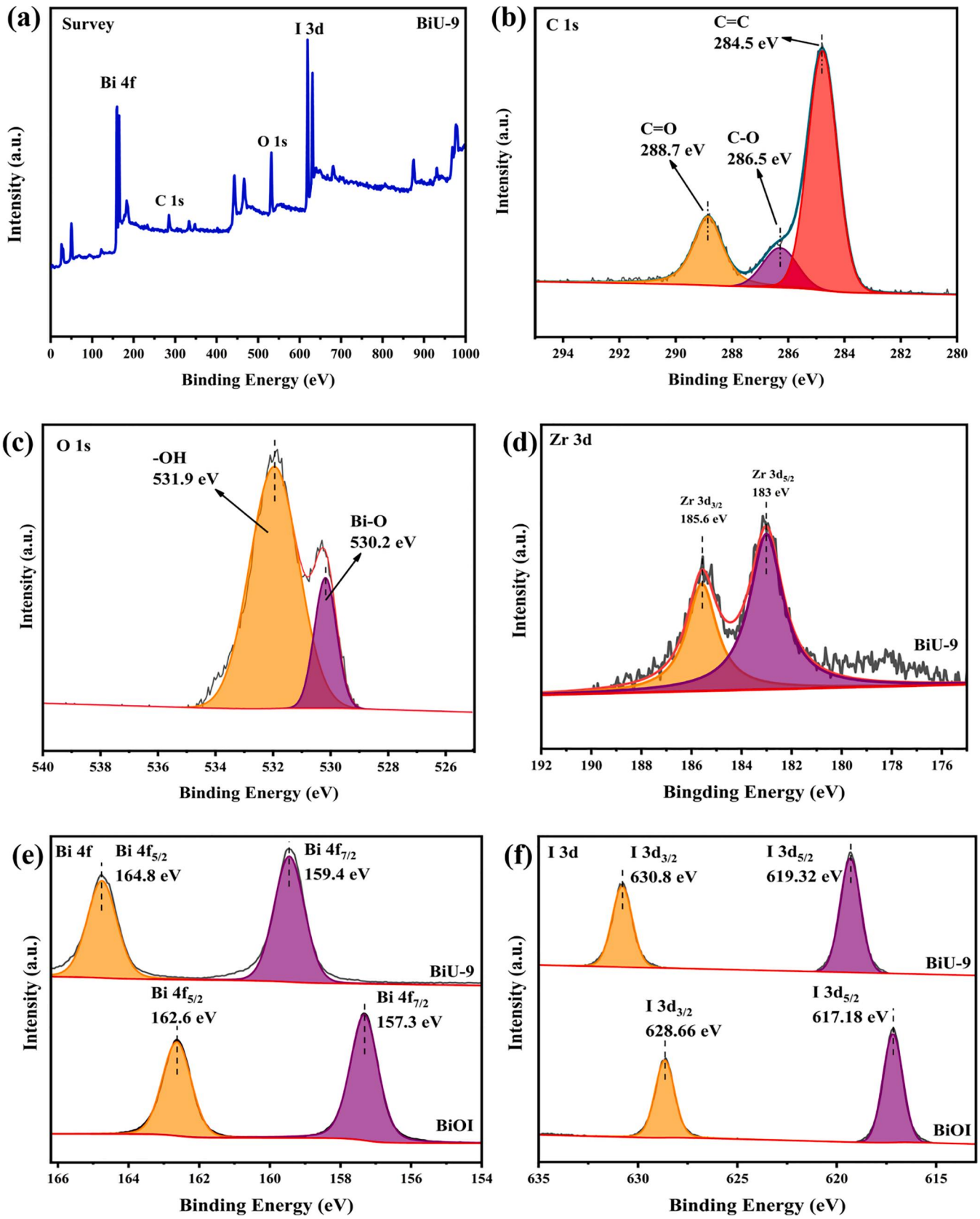

Fig. 4. XPS spectra of the BiU-9 heterojunction. (a) survey, (b) C 1 s, (c) O 1 s, (d) Zr 3d, (e)-(f) Bi 4f and I 3d high-resolution spectra of BiU-9 and pristine BiOI.

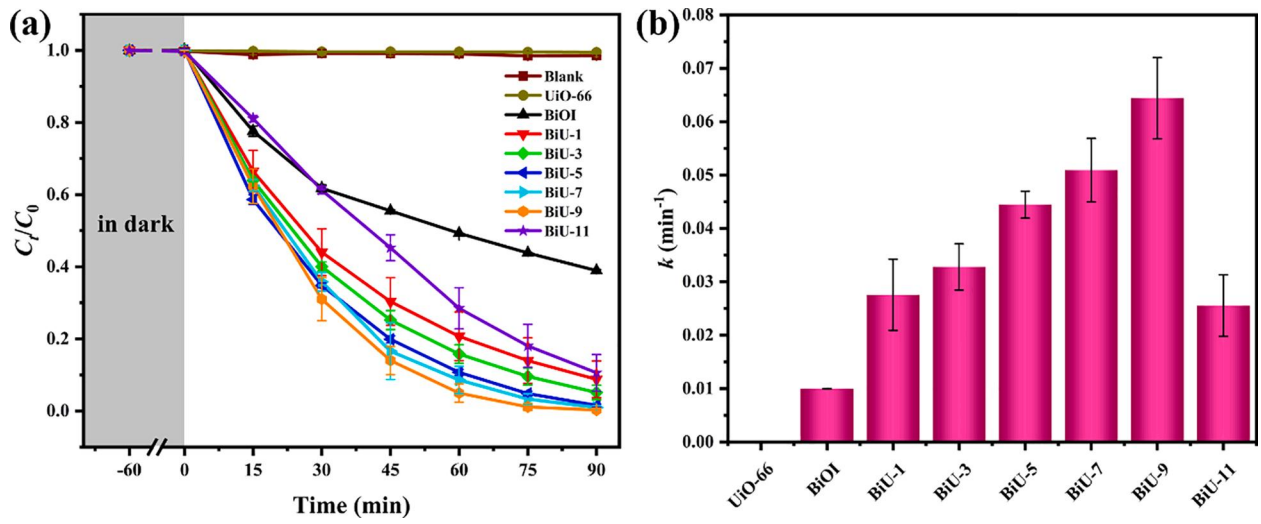

Fig. 5. (a) Photocatalytic degradation of SDZ over UiO-66, BiOI and BiU-*x* heterojunctions under visible light and (b) the reaction rate constants. Condition: SDZ = 5 mg/L, photocatalyst dosage = 0.5 g/L, pH = 5.6.

octahedrons. Therefore, it was reasonable that the close interfacial contact might be contributed to the separation of charge carriers and facilitate a synergetic effect to enhance the photocatalytic activity.

3.1.3. N_2 adsorption and UV–vis DRS analysis

In general, larger specific surface area (S_{BET}) was contributed to promote photocatalytic activity owing to the presence of numerous active sites can absorb and diffuse target organic pollutants via the interconnected porous structure [52]. The N_2 adsorption–desorption isotherms of the prepared materials were depicted in Figure S3. Clearly, UiO-66, BiOI and BiU-*x* heterojunctions exhibited Type IV isotherms on the basis of the IUPAC classification, indicating the existence of mesoporous structures. Furthermore, the shape of the hysteresis loop at high P/P_0 ranging from 0.8 to 1.0 belonged to Type H_3, revealing that the existence of slit-shaped pores on account of aggregation of plate-like samples [53], which can be proved by SEM and TEM results. Moreover, the BET surface areas, average pore sizes and pore volumes of all samples were exhibited in Table S1. The BET specific surface area of pristine BiOI was merely 23.80 m^2/g. However, it can be found that the specific surface areas of the BiU-*x* heterojunctions progressively increased with the increasing of UiO-66 mass percentage, even though they displayed moderate reduction in S_{BET} values as compared to pristine UiO-66. Especially the BiU-11 sample, whose specific surface area reached to 500.99 m^2/g. Hence more active sites would be provided by BiU-*x* heterojunctions to harvest photo-generated charge carriers for further photocatalytic process.

The optical adsorption property was a crucial factor for affecting the photocatalytic activity, in particular with respect to photocatalytic degradation of organic pollutants under visible light irradiation [54]. To explore the light adsorption capacities of pristine UiO-66, BiOI and BiU-*x* heterojunctions, the UV–vis DRS were systematically analyzed, as depicted in Fig. 3(a). As to pristine UiO-66, the adsorption wavelength was about 320 nm, demonstrating that UiO-66 could merely respond to the UV light. However, BiOI displayed a robust photo adsorption capacity ranging from UV to visible light. It was notable that the BiU-*x* heterojunctions exhibited the broader photo adsorption regions and their adsorption capacities for visible light were appreciable as compared to that of pristine UiO-66, which should be attributed to the existence of BiOI in BiU-*x* heterojunctions was inclined to improve the photon response ability. Furthermore, the band gaps (E_g) of the as-prepared samples were also estimated by Kubelka-Munk function Eq. (3) [55]:

$$\alpha h\nu = A\left(h\nu - E_g\right)^{n/2} \quad (3)$$

where *a*, *h*, *v* and A are adsorption coefficient, Planck's constant, frequency of light and a constant, respectively. The n values were decided by the properties of the transition of semiconductors (n = 4 represented indirect transition, whereas n = 1 represented direct transition). According to the reported studies, UiO-66 was subjected to direct transition and the n value was 1 [56], while BiOI can be deemed as indirect transition and its n value can be evaluated as 4 [57]. As depicted in Fig. 3 (b), the E_g values of BiU-1, BiU-3, BiU-5, BiU-7, BiU-9 and BiU-11 were calculated as 1.84, 1.88, 1.89, 1.9, 1.95 and 1.99 eV, respectively, implying that the BiU-*x* heterojunctions were visible-light-driven photocatalysts.

3.1.4. XPS analysis

To manifest the chemical states of the as-prepared BiU-*x* heterojunctions, BiU-9 was chosen as the representative photocatalyst to perform XPS analyses (Fig. 4). As exhibited in Fig. 4(a), the full XPS survey spectrum of the BiU-9 indicated that it was mainly composed of C, O, Zr, Bi and I elements. High-resolution C 1 s, O 1 s, Zr 3d, Bi 4f and I 3d spectra in the BiU-9 were illustrated in Fig. 4(b)-(f). The C 1 s spectrum displayed three peaks centered at 288.7, 286.5 and 284.5 eV, respectively, which can be indexed to the O–C═O, C—O and C—C chemical bonding from UiO-66 [58–60]. The O 1 s spectrum of the BiU-9 in Fig. 4(c) was divided into two peaks at 531.9 eV and 530.2 eV, which can be associated with –OH and Bi–O functional groups, respectively. From Fig. 4(d), the high-resolution Zr 3d spectrum for the BiU-9 can be fitted by two peaks centered at 185.6 and 183.0 eV, which can be ascribed to Zr $3d_{3/2}$ and Zr $3d_{5/2}$, respectively. Furthermore, Fig. 4(e) exhibited two distinct peaks at 164.8 eV and 159.4 eV in the Bi 4f high-resolution spectrum, which were indexed to Bi $4f_{5/2}$ and Bi $4f_{7/2}$, revealing that the valence of Bi in the BiU-9 was + 3 [61,62]. Meanwhile, the I 3d spectrum (Fig. 4(f)) exhibited two distinct peaks at 630.8 eV and 619.3 eV, which corresponded to the I $3d_{3/2}$ and I $3d_{5/2}$ of BiOI, respectively [63]. More importantly, it can be found that the binding energies of Bi 4f and I 3d were shifted toward higher binding energies after combination of UiO-66 octahedrons. This experimental phenomenon provided solid evidence for the strong interfacial contact between UiO-66 and BiOI, the tight growth of BiOI on UiO-66 octahedron might intensively promote the charge carriers separation efficiency in the BiU-*x* heterojunctions.

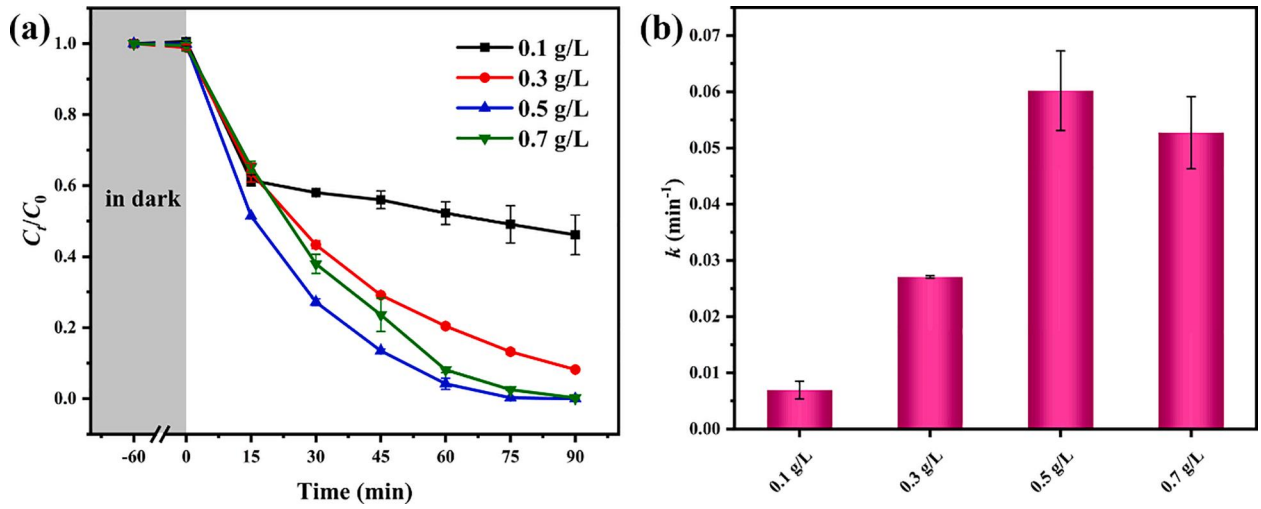

Fig. 6. (a) Photocatalytic degradation of SDZ with different BiU-9 dosages and (b) the reaction rate constants. Condition: SDZ = 5 mg/L, pH = 5.6.

3.2. Evaluation of photocatalytic performance

The photocatalytic performances of the UiO-66, BiOI and BiU-*x* were firstly assessed by SDZ degradation under visible light illumination. It could be seen in Fig. 5(a) that the self-degradation of SDZ can be neglected after 90 min of photocatalysis process. Meanwhile, it was obvious that the SDZ cannot been photodegraded by pristine UiO-66. Moreover, it was obvious that pristine BiOI exhibited relatively low photocatalytic efficiency, only 61.1 % of SDZ can be removed after 90 min visible light irradiation. Nevertheless, the photodegradation efficiencies of SDZ over BiU-1, BiU-3, BiU-5, BiU-7, BiU-9, BiU-11 heterojunctions reached to 94.3 %, 94.9 %, 95.9 %, 98.2 %, 99.9 %, 93.6 % in the same conditions, respectively. For the sake of comparing the quantitative clearly, the pseudo-first-order model of SDZ decomposition was investigated by Eq. (4) [64]:

$$-\ln(C_t/C_0) = kt \quad (4)$$

where k denoted the corresponding degradation rate constant. As exhibited in Fig. 5(b), the photodegradation rates of SDZ over the photocatalysts can be arranged in the order of BiU-9 > BiU-7 > BiU-5 > BiU-3 > BiU-1 > BiU-11 > BiOI > UiO-66. The largest reaction rate constant of BiU-9 heterojunction was 0.0644 min^{-1}, which was 1280 and 2.3 times higher than that of pristine UiO-66 and BiOI, respectively. The above results demonstrated that the presence of an intimate interaction between UiO-66 and BiOI, thus promoting the separation of charge carriers, which were consistent with the above characterization analysis.

3.2.1. Effect of photocatalyst dosage

In general, the kinetic behavior of a photocatalyst on organic pollutants degradation is susceptible to reaction system parameters. Therefore, the influence of BiU-9 dosage (0.1–0.7 g/L) was explored, and the results were illustrated in Fig. 6. As illustrated in Fig. 6(a), the degradation efficiency of SDZ gradually enhanced to the peak value of 99.9 % as the BiU-9 dosage increased from 0.1 to 0.5 g/L. However, when the BiU-9 dosage exceeded 0.5 g/L, the reaction rate dropped dramatically (Fig. 6(b)). This was because the as-prepared BiU-9 not only absorbed photons but also reflected and refracted it. When BiU-9 dosage attained the optimizing level, the visible light transmittance of the reaction system tended to reduce prominently, which may affect the full use of photons and result in weakening photocatalytic efficiency [65]. The turbidities measured in this study for the dosage of BiU-9 raising from 0.1 g/L to 0.7 g/L were 326, 721, 1108 and 1660 NTU, respectively, which further testified the above hypothesis. In addition, the BiU-9 might be inclined to aggregate when its dosage attained a given value [66]. This aggregation could diminish the exposed active sites for photodegradation of SDZ molecules. In addition, we systematically compared the efficacy of the reported photocatalysts for treating SDZ, as shown in, Table 2. Obviously, the as-prepared BiU-9 possessed considerable photocatalytic efficiency and low energy consumption. Considering that the LED lamp has long time, poor heat generation, excellent mechanical stability and without hazardous mercury [67], therefore the constructed BiU-9/LED lamp system was more feasible for actual applications.

3.2.2. Effect of initial solution pH

The photocatalytic efficiency significantly relies on the solution pH owing to it could influence the surface charge property of a photocatalyst, the pollutant state and the formation of reactive oxygen species (ROSs) [77,78]. Therefore, the SDZ removal efficiency was investigated

Table 2
Comparison of the SDZ photocatalytic degradation performances accomplished by the previous reported photocatalysts.

Photocatalyst	SDZ concentration (mg/L)	Irradiation time (min)	Dosage (g/L)	Efficiency (%)	Lighting equipment	Reference
$Zn_3(PO_4)_2/BiPO_4$	10	240	1	99	35 W UV–C lamp	[61]
g-C_3N_4/carbon dots	2.5	60	0.4	100	500 W Xe lamp	[68]
Cv-CNNs	10	90	0.2	100	300 W Xe lamp	[69]
$Zn_{1-x}Mg_xFe_2O_4$	10	90	0.3	100	300 W Xe lamp	[70]
AQ2S@rGO	10	150	0.1	100	300 W Xe lamp	[71]
Au-BiOBr-Co_3O_4	20	120	1	100	300 W Xe lamp	[72]
Ag/S-$BiVO_4$	5	240	1	100	500 W Xe lamp	[73]
$BiVO_4/NaBiO_3$	10	60	0.2	94	500 W Xe lamp	[74]
TiO_2	10	90	1	100	300 W Xe lamp	[75]
Fe_3O_4/BiOI	20	120	1	85	300 W Xe lamp	[76]
BiU-9	5	90	0.5	100	5 W LED visible light	This work

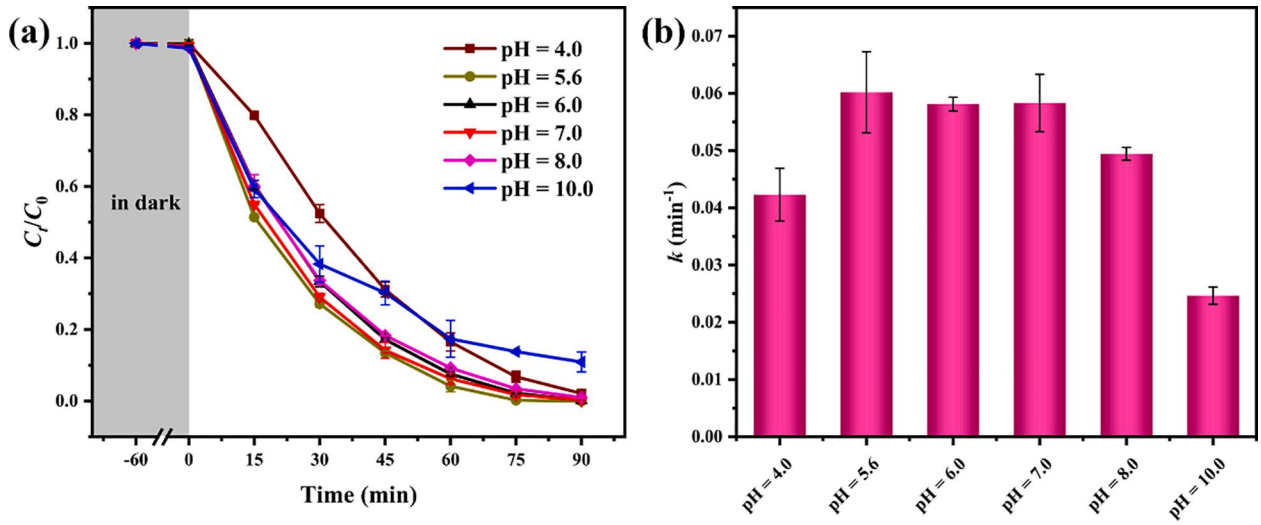

Fig. 7. (a) Effects of various initial pH values on SDZ removal, (b) the reaction rate constants. Condition: SDZ = 5 mg/L, BiU-9 = 0.5 g/L.

when the initial pH values ranged from 4.0 to 10.0. The SDZ concentration and BiU-9 dosage maintained at 5 mg/L and 0.5 g/L, respectively. As exhibited in Fig. 7(a), the effect of initial pH on the adsorption of SDZ over the BiU-9 was negligible, which was quite different from previous studies about SDZ photodegradation [79,80]. According to the pK_{a1} and pK_{a2} values of SDZ were 1.57 and 6.5, respectively [81]. Therefore, when the solution pH was between 4.0 and 10.0, the SDZ molecules were uncharged or negatively charged (the pH-dependent states of SDZ could be expressed as the Eq. (5)). As shown in Figure S4, the point of zero charge (pH_{pzc}) of BiU-9 was approximately 3.15, indicating that the surface of BiU-9 was negatively charged when pH values above 3.15. Hence the SDZ adsorption capacities over the BiU-9 at different pH values were extremely weak due to the electrostatic repulsion.

Apparently, the photodegradation efficiencies of SDZ at pH values being 4.0–10.0 could reach up to 99.9 % after 90 min of visible light illumination, suggesting that decomposition of SDZ by the as-prepared BiU-9 worked efficiently over a relatively wide pH range. As shown in Fig. 7(b), the k values followed the order of pH = 5.6 (0.06019 min^{-1}) > pH = 7.0 (0.05833 min^{-1}) > pH = 6.0 (0.05812 min^{-1}) > pH = 8.0 (0.04944 min^{-1}) > pH = 4.0 (0.0423 min^{-1}) > pH = 10.0 (0.02466 min^{-1}). At the pH range of 5.6–7.0, the SDZ molecule was neutrally charged, which might promote it to interact with the –OH groups from BiU-9 via surface OH–π interactions or transition-metal cation–π interactions [82]. Therefore, the improved interaction between SDZ and the surface functional groups from BiU-9 made the photocatalytic reaction more efficient at the pH range of 5.6–7.0. Meanwhile, it can be observed that the photocatalytic efficiencies were inclined to decline at pH = 4.0 and 10.0, which was mostly because the abundant H^+ ions at acidic condition might lead to the more consumption of $\cdot O_2^-$ generated during the photocatalytic process, as shown in Eq. (6) [83]. Normally, a growing pH was conducive to the generation of more ·OH via Eq. (7) [84]. Nonetheless, a decrease in the photocatalytic performance was seen at pH = 10.0, revealing the ·OH played a minor role for SDZ decomposition. On the other side, as the pH values raised up, the oxidizing capacity of the photo-generated h^+ will be decreased owing to its electro-positivity [85].

$$\cdot O_2^- + 2H^+ + e^- \rightarrow H_2O_2 \quad (6)$$

$$h^+ + OH^- \rightarrow \cdot OH \quad (7)$$

3.2.3. *Effect of co-existing matters*

As is well known, the real wastewater contains a mass of inorganic anions, and those inorganic anions play important roles in photocatalytic process [86]. Therefore, the effect of Cl^-, SO_4^{2-}, NO_3^- and HCO_3^- on the photodegradation of SDZ was investigated with the aid of Box-Behnken experimental design methodology. In detail, Cl^-, SO_4^{2-}, NO_3^- and HCO_3^- were denoted as 4 experimental variables *A*, *B*, *C* and *D*. According to the background concentrations of the above anions in real industrial pharmaceutical wastewater [33,34]. Table S2 (a total of 29 runs) showed the effects of various variables on the SDZ removal efficiency over the BiU-9 under visible light illumination. More critically, a quadratic polynomial model was acquired to quantitatively estimate the relationship between the response (Efficiency%) and independent variable, as described in Eq. (8):

$$\begin{aligned}\text{Efficiency\%} = {} & 69.78 - 5.05A - 3.11B - 0.4C - 8.2D + 0.12AB \\ & - 0.05AC + 0.41AD + 0.23BC + 0.045CD + 0.17A^2 \\ & + 0.14B^2 - 0.77C^2 - 1.29D^2\end{aligned} \quad (8)$$

To determine the satisfactoriness of the predicted model, the ANOVA analysis was also conducted in this study. As shown in Table S3, significant parameter (p-value) of the obtained model was < 0.0001, and the R^2 and $R^2_{adjusted}$ values were 0.99 and 0.98, respectively, implying that the predicted data were consistent with the predicted data. More importantly, on the basis of the *F*-values of variables, a conclusion can be drawn that the effects of four variables on SDZ degradation followed the order of: *D* (1083.12) > *C* (409.93) > *A* (155.92) > *B* (2.61), revealing that the inhibition effect of these anions was in the order as follows: $HCO_3^- > NO_3^- > Cl^- > SO_4^{2-}$. Furthermore, interference degree of co-existing anions on degradation of SDZ over BiU-9 under visible light irradiation can be explained as the following. Fig. 8(a) showed the effect of HCO_3^- and Cl^- on the SDZ removal efficiency while the concentrations

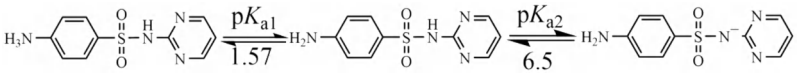

(5)

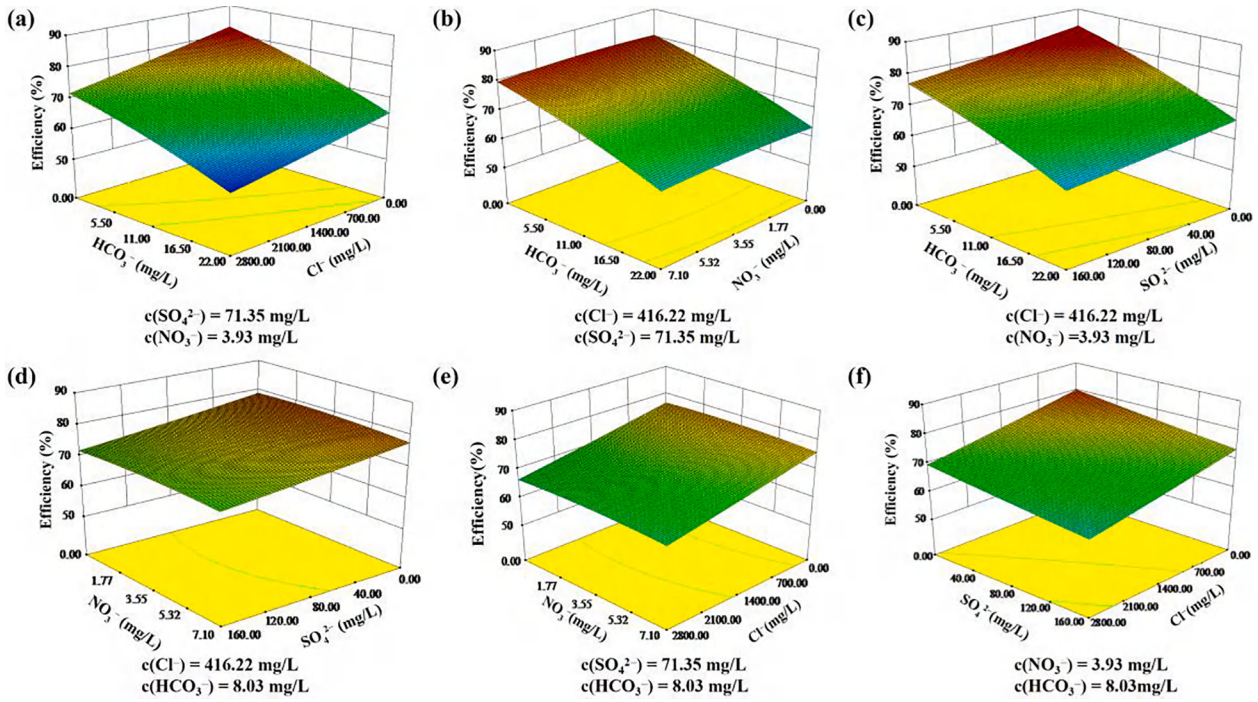

Fig. 8. 3D plots of binary interaction of co-existing anions (Cl^-, SO_4^{2-}, NO_3^- and HCO_3^-) versus photocatalytic efficiency of BiU-9.

of SO_4^{2-} and NO_3^- were maintained at 71.35 and 3.93 mg/L, respectively. Apparently, the removal efficiency decreased as the concentrations of HCO_3^- and Cl^- simultaneously increased. Similar trends could also be found in Fig. 8(b) and (c), in which the photocatalytic degradation efficiencies also remarkably decreased when the concentrations of HCO_3^-, NO_3^- and SO_4^{2-} increased. This result indicated that the co-existence of HCO_3^- could display a considerable antagonistic effect in SDZ removal compared with the photocatalytic reaction system contained the above anions individually. Fig. 8(d) depicted the effect of NO_3^- and SO_4^{2-} concentrations on the removal efficiency for HCO_3^- and Cl^- concentrations of 8.03 mg/L and 416.22 mg/L, respectively. Because the increasing NO_3^- concentration was less significant for SDZ removal in comparison to the increasing of HCO_3^- concentration, thus the increasing concentrations of NO_3^- and the other co-existing anions had less antagonistic effect in photocatalysis process. Similar trend can also be found in Fig. 8(e), in which the variables of RSM were NO_3^- and Cl^-. Fig. 8(f) displayed the effect of SO_4^{2-} and Cl^- concentrations on the removal efficiency. It was not difficult to find that the removal efficiency was also reduced to some extent as the concentrations of SO_4^{2-} and Cl^- increased. Based on the RSM analysis, the maximum photodegradation efficiency will be achieved by providing the minimum concentrations of inorganic anions.

As a whole, the pervasive inhibitory phenomena can be attributed to the electrostatic repulsion effect (Fig. 8). With the increasement of the above anions, the electrostatic repulsion effect will be strengthened, thus weakening the adsorption capacity of the as-prepared BiU-9. It should be noted that obvious inhibition effect happened for HCO_3^-, it was mainly due to the solution pH significantly increased with the addition of HCO_3^-, which can remarkably impair the photocatalytic efficiency. Previous studies suggested that HCO_3^- played an important role in scavenging ·OH as illustrated in Eq. (9). As mentioned in section 3.2.2, ·OH hardly worked in this reaction system, thus the change of pH was the key factor affecting the photocatalytic efficiency. With respect to NO_3^-, it can consume photo-generated electrons [87], leading to reduce yield of ROSs, such as $\cdot O_2^-$, which might possess strong oxidation capacity for SDZ decomposition. And Cl^- might act as scavengers for the photo-generated holes as illustrated in Eq. (10) [88]. Although the formed Cl· radical had a considerable reactivity, it was less reactive than holes, thereby reducing the photocatalytic activity.

$$HCO_3^- + \cdot OH \rightarrow \cdot CO_3^- + H_2O \quad (9)$$

$$Cl^- + h^+ \rightarrow Cl\cdot \quad (10)$$

Previous studies also suggested that natural organic matter (NOM) in water environments influences the effectiveness in photocatalytic degradation of target organic pollutants through inner filter effect, ROSs scavenging and competitive adsorption [89–91]. Therefore, the SDZ photodegradation efficiencies affected by humic acid (HA) in water were shown in Figure S5(a). The photocatalytic efficiencies decreased with the increase of HA concentrations (2.5–10.0 mg/L). And the reaction rate dropped to 0.0086 min^{-1} when the co-existing HA concentration reached to 10 mg/L (Figure S5(b)), which was also found in the previous studies for the oxidation of sulfanilamide antibiotics by other types of photocatalysts [92,93]. As mentioned in 3.2.2, the SDZ adsorption capacity over the BiU-9 was extremely weak due to the electrostatic repulsion, implying that there was no obvious competitive adsorption between SDZ and HA. Therefore, the inhibitory effect of HA was attributed to that the HA can react with the ROSs due to the non-selective nature of the ROSs and reduced effectiveness of the ROSs in the corresponding photocatalytic process.

3.2.4. *Evaluation of actual application performance*

To further asses the real application potential of the constructed reaction system, the photocatalytic activities of pristine UiO-66, BiOI and BiU-9 were investigated under real sunlight illumination. As depicted in Fig. 9(a), the self-degradation of SDZ under real sunlight was negligible. However, when the above photocatalysts were added, the SDZ photodegradation efficiencies greatly increased to 62.0 % and 73.6 % for pristine UiO-66 and BiOI, respectively. Obviously, the BiU-9 exhibited higher photocatalytic activity to SDZ, approximately 100 % of SDZ was removed within 60 min of sunlight irradiation. The above results might be ascribed to the broad-spectrum of sunlight, especially the involvement of UV light, which was further testified by the UV–vis DRS spectra of UiO-66, BiOI and BiU-*x* heterojunctions (Fig. 3(a)). Therefore, it revealed that the BiU-*x* heterojunctions can be deemed as potential sunlight-driven photocatalysts.

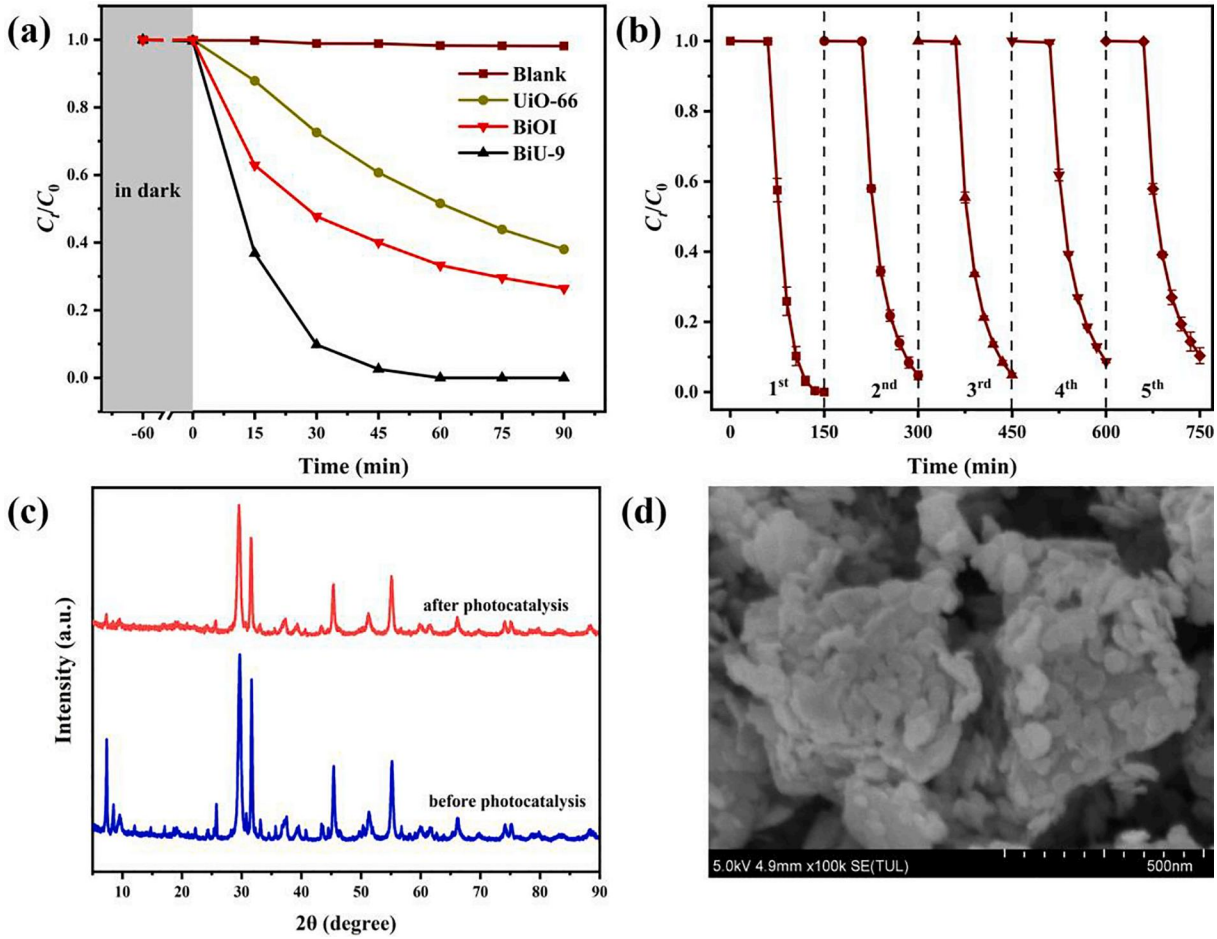

Fig. 9. (a) Photocatalytic degradation of SDZ over pristine UiO-66, BiOI and BiU-9 under real sunlight irradiation and (b) cyclic experiment for photodegradation of SDZ over the BiU-9 under visible light illumination; (c)-(d) PXRD and SEM image of the BiU-9 before and after the cycling experiment.

Meanwhile, the stability and reusability of a given photocatalyst are essential for its actual applications. Thus, the stability test of representative BiU-9 was assessed under visible light irradiation. As illustrated in Fig. 9(b), it was fascinating that no remarkable decrease was found in SDZ removal efficiency after 5 consecutive operations, and the corresponding photocatalytic efficiency also reached above 90 %. Furthermore, possible structural and surface change of BiU-9 were investigated before and after cyclic runs. As shown in Fig. 9(c), the fresh and used samples displayed similar PXRD patterns, suggesting that the BiU-9 retained its framework structure. XPS spectra (Figure S6) confirmed that the BiU-9 had no obvious structural and surface change after 5 runs in contrast to the fresh sample. Meanwhile, it can be found that the BiU-9 still kept its nanoplate-on-octahedral heterostructure (Fig. 9(d)), indicating that the as-prepared BiU-*x* heterojunctions were promising in actual photocatalysis application for environmental remediation.

3.3. Photocatalytic mechanism

The recombination property of photo-generated electron-hole pairs is a key parameter that determines the photocatalytic performance [94–97]. Hence PL, photocurrent responses and EIS analysis were implemented. Firstly, the PL spectra of the as-prepared photocatalysts were carried out to explore the recombination characteristics of charge carriers, as shown in Fig. 10(a). Obviously, the PL intensities emitted by BiU-*x* heterojunction were weaker than those of pristine UiO-66 and BiOI, suggesting that more sufficient migration and transfer of electrons and holes were achieved in BiU-*x* photocatalysts to boost the photocatalytic SDZ elimination. Furthermore, as the BiU-9 sample displayed the lowest PL signal, revealing that it exhibited better charge carrier separation than the other BiU-*x* heterojunctions. Secondly, to deepen understanding of photo-generated carriers separation behavior, photocurrent response curves of UiO-66, BiOI and the BiU-9 heterojunction were measured during on/off light illumination for three cycles (Fig. 10(b)). As the light turned on, the maximal photocurrent densities generated by UiO-66 and BiOI were merely 0.0196 and 0.625 μA/cm^2, respectively. Intriguingly, the as-prepared BiU-9 heterojunction displayed improved photocurrent density, revealing that more available charges could effectively contribute to the photodegradation process. Thirdly, EIS curves was also applied to study the interface charge resistance of different photocatalysts [98]. Normally, a smaller semicircle diameter in the EIS spectra suggests a lower charge impedance. As shown in Fig. 10(c), the BiU-9 possessed the smallest arc radius among all the photocatalysts, indicating the fastest interfacial charge transfer and maximum separation efficiency of electron-hole pairs were achieved by the BiU-9. Based on the aforementioned characterizations, it can be concluded that the fabrication of heterojunction between UiO-66 and BiOI was conducive to suppress the recombination of charge carriers, thereby improving the photocatalytic efficiency.

The reactive species are of crucial importance for the heterogeneous catalytic process, the radical capture experiment was reasonably designed and used to ascertain the dominating species for SDZ removal and reveal the photodegradation mechanism. As shown in Fig. 10(d), TEA, *p*-BQ, L-Histidine and TBA were selected to scavenge of h^+, $\cdot O_2^-$, $^1O_2$ and ·OH reactive species, respectively [99,100]. The SDZ

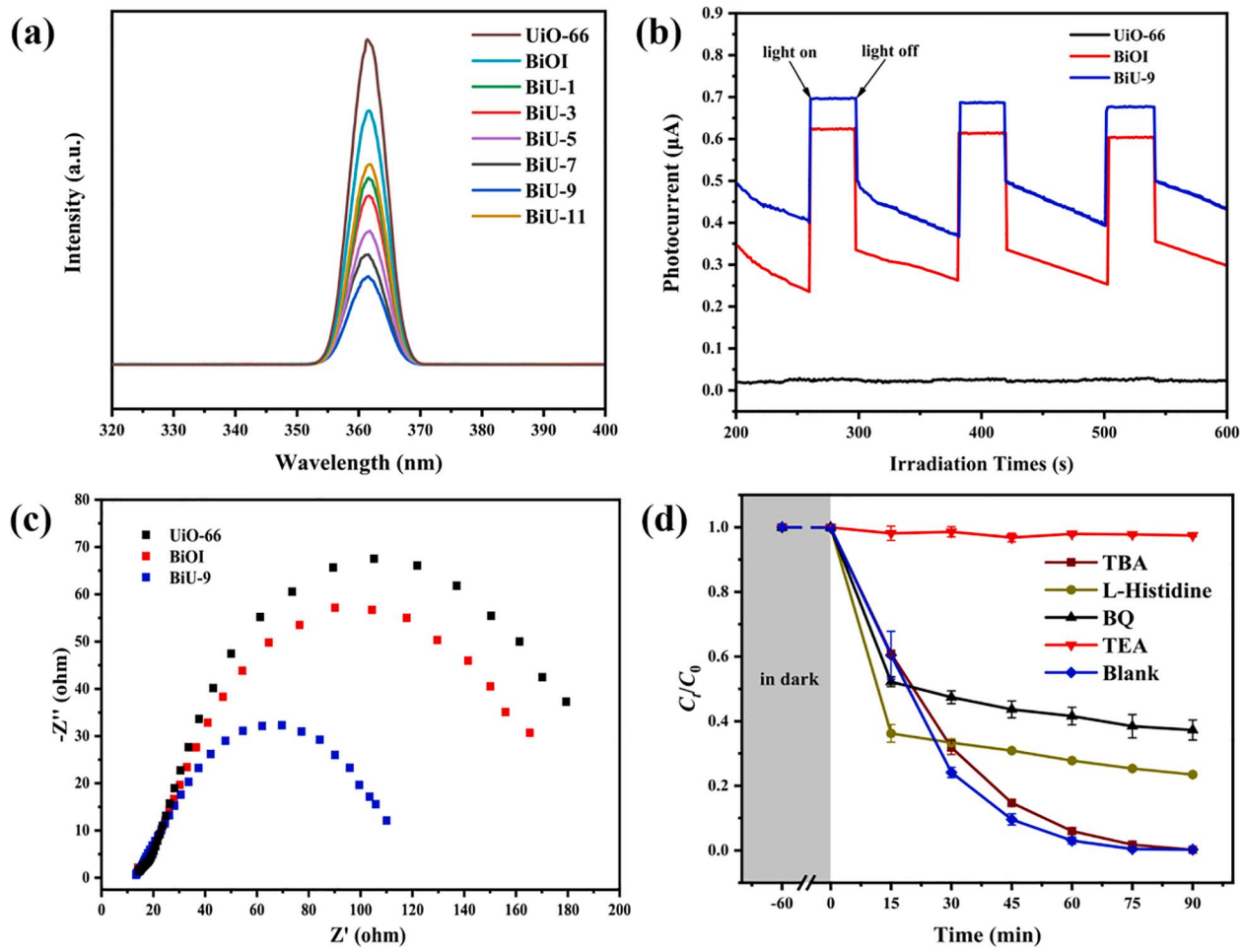

Fig. 10. (a) Steady-state PL spectra of pristine UiO-66, BiOI and BiU-*x* heterojunctions, (b) photocurrent response densities and (c) EIS Nyquist plots of UiO-66, BiOI, BiU-9, (d) photocatalytic degradation of SDZ over the BiU-9 with the presence of various scavengers.

degradation efficiency decreased dramatically after introducing TEA, suggesting that h^+ dominated the degradation of SDZ over the BiU-9. Furthermore, the SDZ removal efficiency reduced to some degree with the addition of *p*-BQ and L-Histidine, suggesting that $\cdot O_2^-$ and $^1O_2$ were also involved in the removal of SDZ. However, the presence of TBA had a negligible inhibition on the decomposition of SDZ, revealing that ·OH was not the main free radical for removal of SDZ. These results were consistent with the analysis about the influence of pH on photocatalytic process.

In addition, the Mott-Schottky curves were tested to confirm the semiconductor types and identify the flat band potential (E_{fb}) of UiO-66 and BiOI, respectively [101]. Generally, the E_{fb} can be obtained according to the Eqs. (11) and (12) [102]. The ε_0 and ε represented the vacuum dielectric constant and relative dielectric constant. N_d, e, C, N_a, E, K_B and T were the donor density, electronic charge, interface capacitance, acceptor density, applied potential, Boltzamann constant and absolute temperature, respectively. As shown in Fig. 11(a)-(c), the E_{fb} values of UiO-66, BiOI and BiU-9 were determined to be −1.04, 1.5 and −0.78 eV *vs.* Ag/AgCl, respectively. More importantly, the positive slope proved that UiO-66 belonged to n-type semiconductor, whereas the negative slope confirmed the p-type property of BiOI. As it can be deemed that E_{fb} of a semiconductor is equal to its Fermi level (E_F) [25]. Thus based on the Nernst formula (Eq. (13) [103], the E_F values of UiO-66, BiOI and BiU-9 were calculated as −0.843, 1.697 and −0.583 eV *vs.* NHE. To ascertain the band alignments of pristine UiO-66 and BiOI, the VB-XPS spectra were used to measure their highest occupied molecular position (E_{HOMO}) and valence band position (E_{VB}) (Fig. 11(d)). And the corresponding normal hydrogen electrodes were calculated by the Eq. (14) [104], where Φ and $E_{VB\text{-}XPS}$ referred to electron work function of the analyzer and the value of valence band maximum. Therefore, E_{HOMO} and E_{VB} of UiO-66 and BiOI were calculated as 3.06 and 1.94 eV *vs.* NHE. By means of the Eq. (15), the E_{LUMO} and E_{CB} of UiO-66 and BiOI were −0.88 and 0.18 eV *vs.* NHE, respectively.

$$C^2/1 = 2/e\varepsilon\varepsilon_0 N_d(E - E_{fb} - K_B T/e) \quad n-type \tag{11}$$

$$C^2/1 = 2/e\varepsilon\varepsilon_0 N_a(E - E_{fb} - K_B T/e) \quad p-type \tag{12}$$

$$E_{NHE} = E_{Ag/AgCl} + 0.197 \tag{13}$$

$$E_{VB(HOMO)} = \Phi + E_{VB-XPS} - 4.44 \tag{14}$$

$$E_g = E_{VB(HOMO)} - E_{CB(LUMO)} \tag{15}$$

On the above bases, the credible reaction mechanism for the photodegradation of SDZ over BiU-*x* photocatalyst was illustrated in Fig. 12. Prior to possessing any contact, the band alignment between UiO-66 and BiOI can be classified as type I lineup, which was detrimental to efficient separation of photo-generated charge carriers, thus contradicting with obtained photoelectrochemical analysis. However, after contact, the BiU-*x* p-n heterostructure was built. By reason of the discrepancy in their E_F values, the E_F tended to shift to achieve a new equilibrium (−0.583 eV *vs.* NHE) and their band structures will be subsequently rearranged [105]. As a result, an IEF at the interface between UiO-66 and BiOI could be formed, making BiOI negatively charged and UiO-66 positively

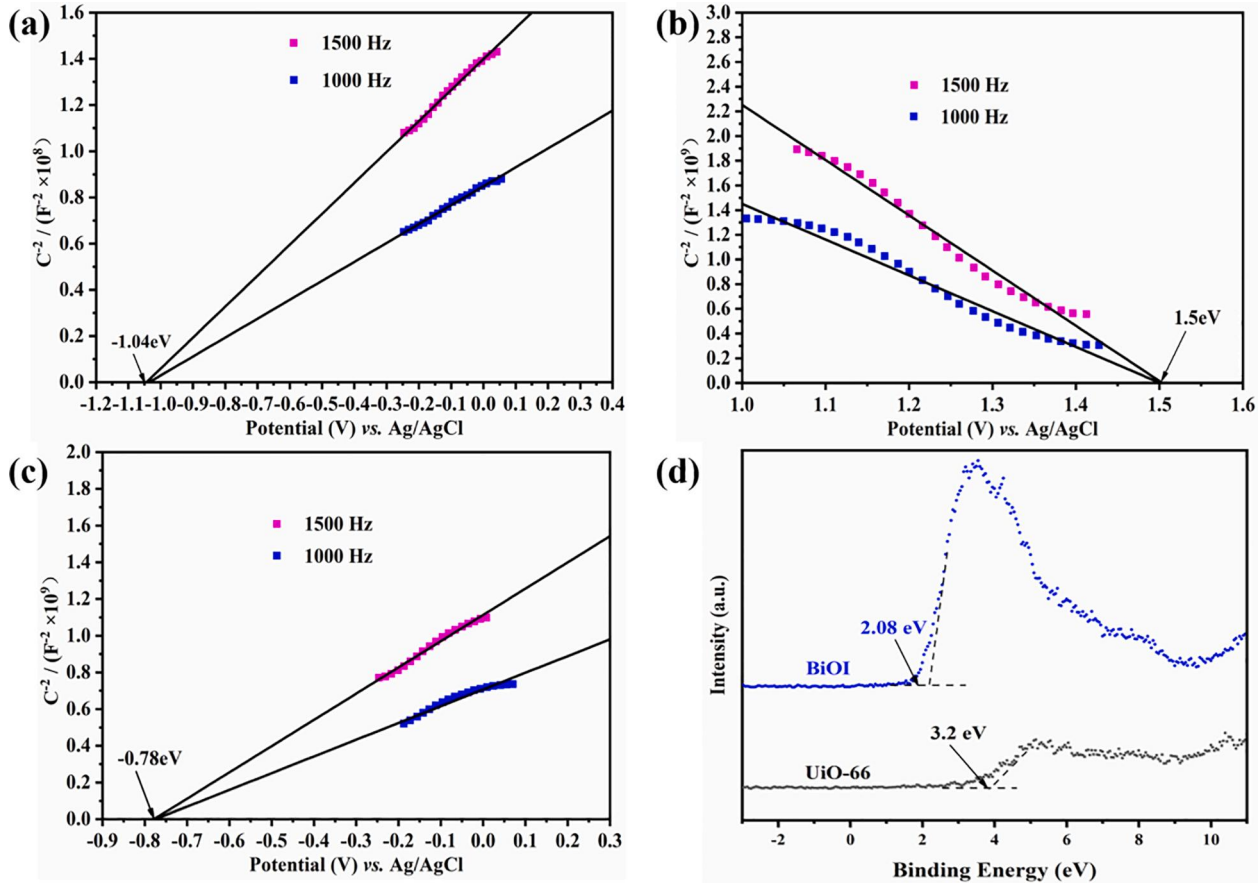

Fig. 11. Mott-Schottky curves of (a) UiO-66, (b) BiOI and (c) BiU-9; (d) VB-XPS spectra of UiO-66 and BiOI.

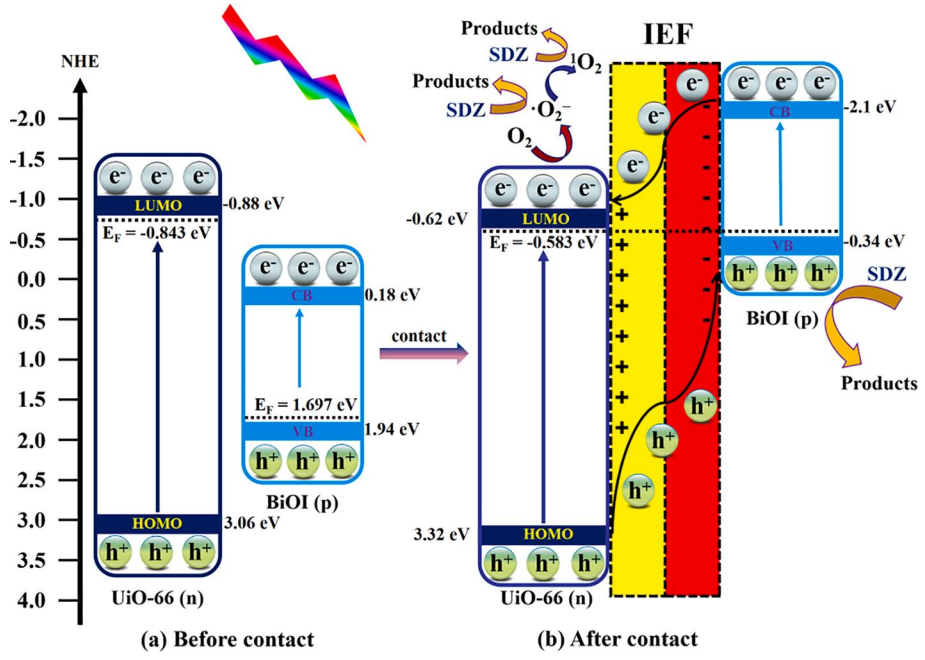

Fig. 12. Possible photocatalysis enhancement mechanism of the BiU-*x* p-n heterojunctions.

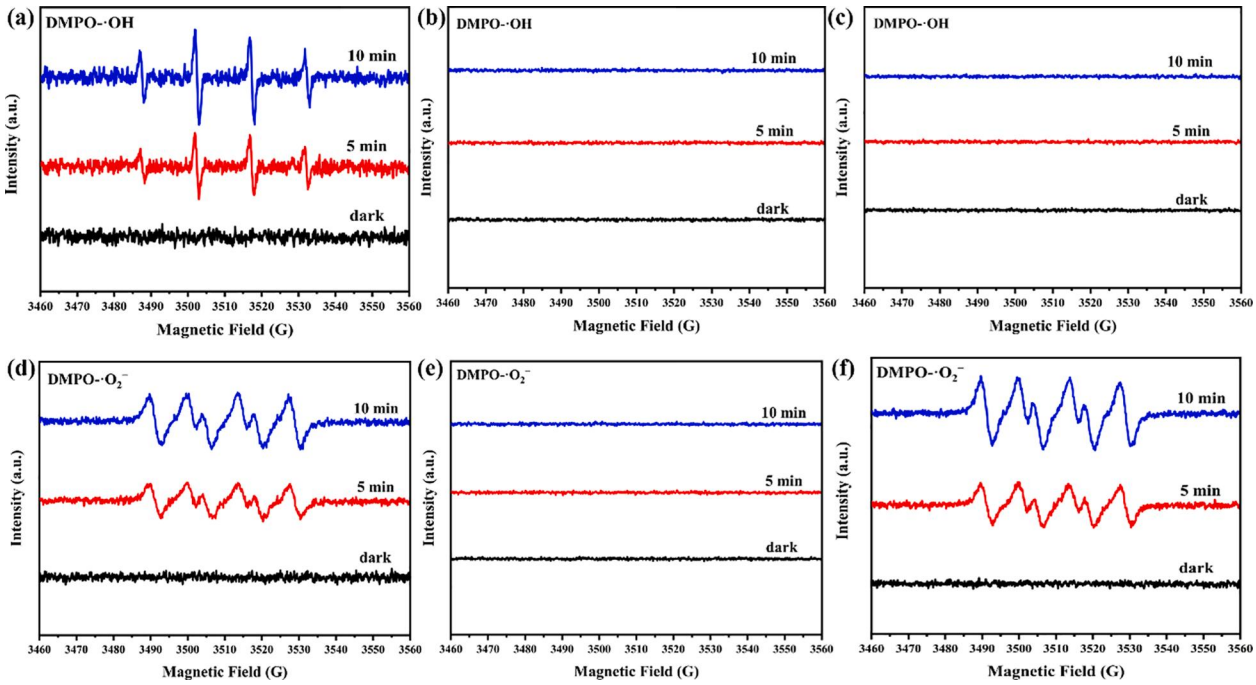

Fig. 13. DMPO-·OH and DMPO-·O_2^- adducts detected by ESR technique. (a, d) UiO-66, (b, e) BiOI and (c, f) BiU-9.

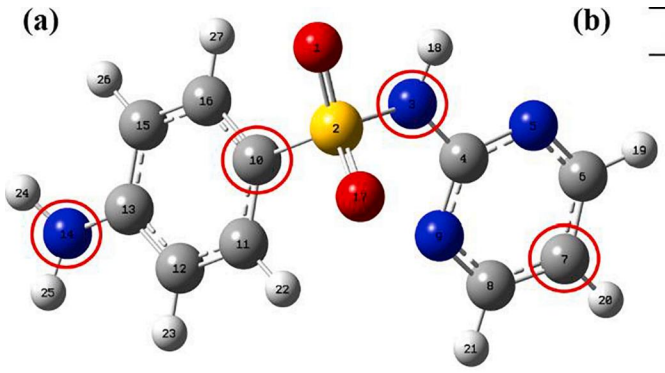

Atom	No	Charge (0)(e/Å3)	Charge (-1)(e/ Å3)	Charge (+1)(e/ Å3)	f^-
O	1	-0.94782	-0.98107	-0.89702	0.0508
S	2	2.32443	2.32014	2.305	-0.01943
N	3	-0.88598	-0.90023	-0.81064	0.07534
C	4	0.58427	0.58428	0.57408	-0.01019
N	5	-0.50752	-0.59571	-0.46365	0.04387
C	6	0.06202	-0.0802	0.07344	0.01142
C	7	2.931	-0.34818	-0.2767	0.07676
C	8	2.864	-0.06167	0.07273	0.00696
N	9	-0.35346	-0.58811	-0.49592	0.01501
C	10	-0.37422	-0.42069	-0.25753	0.11669
C	11	-0.17532	-0.1772	-0.17727	-0.00195
C	12	-0.28648	-0.32605	-0.21655	0.06993
C	13	0.18268	0.11045	0.21397	0.03129
N	14	-0.84505	-0.89919	-0.68584	0.15921
C	15	-0.28494	-0.31714	-0.21909	0.06585
C	16	-0.18691	-0.18543	-0.18607	0.00084
O	17	-0.91795	-0.93937	-0.86241	0.05554

Fig. 14. (a) The chemical structure and (b) Fukui index and NPA charge distribution of SDZ.

charged at the interfacial area. When BiU-*x* photocatalysts absorbed luminous energy from light sources, the electrons and holes were generated from UiO-66 and BiOI (Eqs. (16)–(18)). Since the E_{CB} and E_{VB} of BiOI were more negative than that of UiO-66, the photo-generated electrons in BiOI were inclined to thermodynamically move to the LUMO of UiO-66, whereas the photo-generated holes in the HOMO of UiO-66 thermodynamically injected into the VB of BiOI. Being compared with the standard reaction potential of $O_2/\cdot O_2^- = -0.33$ eV *vs.* NHE [106], the electrons gathered on the LUMO of UiO-66 (-0.62 eV *vs.* NHE) were still negative enough to react with O_2 to yield $\cdot O_2^-$ radicals (Eq. (19)). Nonetheless, the holes on the VB of BiOI were incapable of generating ·OH due to its E_{VB} (−0.34 eV *vs.* NHE) was less positive than the oxidation potential of $OH^-/\cdot OH = 2.40$ eV *vs.* NHE [107], which was consistent with pH-influence and radical trapping experiments. Furthermore, ESR was introduced to validate the generation of $\cdot O_2^-$ and ·OH over different photocatalysts. As to pristine UiO-66, DMPO-·OH and DMPO-·O_2^- adducts can be detected under Xe lamp illumination (Fig. 13), revealing that $\cdot O_2^-$ and ·OH were reasonably generated for UiO-66 upon photoexcitation process. Oppositely, negligible DMPO-·OH and DMPO-·O_2^- signals were captured in the ESR spectra of BiOI. As to BiU-9, only the DMPO-·O_2^- adduct can be detected by ESR technique, verifying ·OH could be excluded from this reaction system. Besides, under such circumstances, a portion of $\cdot O_2^-$ might react with photo-generated electrons to generate $^1O_2$ [108], as illustrated in Eq. (20), which also participated the SDZ removal. At the same time, the holes congregated on the VB of BiOI triggered the direct oxidation of SDZ owing to its considerable oxidative capability. In brief, by virtue of p-n heterojunction, the BiU-*x* photocatalysts exhibited good potential in treating pharmaceutical antibiotics.

$$\text{BiU} - x + h\nu \rightarrow \text{BiU} - x\ (h^+\ ,\ e^-) \quad (16)$$

$$e^-(\text{BiOI}) + \text{UiO-66} \rightarrow \text{UiO-66}\ (e^-) \quad (17)$$

$$\text{BiOI} + h^+\ (\text{UiO-66}) \rightarrow \text{BiOI}\ (h^+) \quad (18)$$

$$O_2 + e^- \rightarrow \cdot O_2^- \quad (19)$$

$$\cdot O_2^- + e^- \rightarrow {}^1O_2 \quad (20)$$

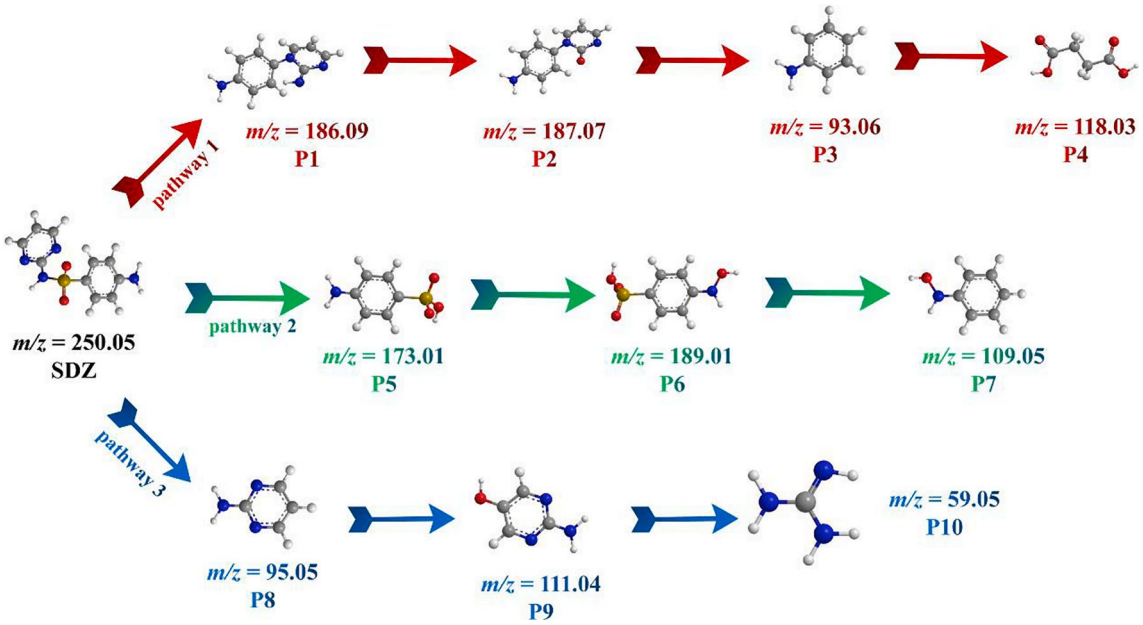

Fig. 15. Proposed pathways for SDZ degradation in the BiU-9 photocatalytic process.

$$h^+/\cdot O_2^-/^1O_2 + SDZ \rightarrow CO_2 + H_2O + \text{Small molecules} \quad (21)$$

3.4. SDZ degradation pathway, DFT calculation and ecotoxicity analysis

To predict the SDZ degradation pathway more accurately and considering that the dominant reactive species in this reaction system were h^+, $\cdot O_2^-$, $^1O_2$, DFT calculations were used to obtain the Fukui index based on electrophilic attack (f^-) on the basis of natural population analysis (NPA) charge distribution of SDZ molecule. From Fig. 14(a)-(b), the C10 (0.11669), N14 (0.15921), C7 (0.07676) and N3 (0.07534) sites exhibited a relatively high f^- values. Combined with the Fukui index and photodegradation intermediates resolved by LC-MS, three reliable photocatalytic degradation pathways of SDZ were depicted in Fig. 15.

In the first pathway, reactive h^+ was inclined to attack the S—N bond of SDZ, resulting in a structural rearrangement to generate compound *P*1 [109,110]. Subsequently, the formed P1 might be attacked by $\cdot O_2^-$ radicals to form the intermediate P2. Then the C—N bond of P2 between aniline and 2-oxoprimidine was ruptured by h^+, which was beneficial to the transformation of intermediate P3. The intermediate P4 could be generated from the P3 via a ring-opening process under the oxidation reaction of h^+, $\cdot O_2^-$ and $^1O_2$ reactive species.

In the second pathway, the $\cdot O_2^-$ radicals also preferred to attack the S—N bond of SDZ molecule as N3 possessed a relatively high f^- value, which led to generate hydroxylated compound P5. Considering that the f^- value of N14 was up to 0.15921, thus P5 can produce the intermediate P6 due to electrophilic $\cdot O_2^-$ attack of amino groups. Considering that the C10 displayed the second highest f^- value of 0.11669, revealing that C—S bond in P6 was highly vulnerable to electrophilic attack. Hence the P6 will be directly ruptured by h^+ to generate P7.

In the third pathway, under the attack of h^+, SDZ molecule can be transformed into the intermediate P8. Subsequently, the presence of $\cdot O_2^-$ and $^1O_2$ reactive species were tended to attack the aromatic rings via the electrophilic effect, and then the compound P9 could be thereupon formed with the aid of hydroxylation process. Finally, after the ring-opening process, the intermediate P9 was further cracked to the P10. More importantly, as the photodegradation process continued, the above small organics will ultimately be decomposed into CO_2 and H_2O.

The bioaccumulation factor and developmental toxicity of SDZ and the corresponding intermediates were assessed through Toxicity Estimation Software (T.E.S.T.) [111]. It was obvious that a large proportion of the intermediates showed lower values of bioaccumulation factor (Figure S7(a)), suggesting the process of SDZ photodegradation was also accompanied by the detoxification effect. Moreover, it was worth noting that the developmental toxicity index of SDZ was 0.9, meaning that it can be deemed as a "developmental toxicant". But a great number of photocatalytic degradation products showed relatively lower values of developmental toxicity (Figure S7(b)). Comprehensive results showed that photocatalytic process over BiU-*x* heterojunctions system can not only efficient degradation of SDZ, but also reduce its ecotoxicity. Thus, the constructed photocatalytic system can be considered as a "green" technology due to its property of toxicity attenuation, revealing huge actual potential in eliminating SDZ in water environments.

4. Conclusions

In summary, a series of BiU-*x* heterojunctions with nanoplate-on-octahedral heterostructure were firstly fabricated via a controlled precipitation method, which overcame the shortcomings of traditional preparation methods for fabricating MBCs, such as the requirement of high temperature and pressure. The *in-situ* deposition of p-type BiOI nanoplates on the surface of n-type UiO-66 octahedrons can effectively inhibit the electron-hole recombination and distinctly broaden the visible-light adsorption region, thus resulting in the remarkable photocatalytic activity towards the SDZ photodegradation under low-power visible light and real sunlight. The trapping experiments and ESR analysis corroborated the significant roles of h^+ and $\cdot O_2^-$ in the SDZ removal. Wide pH operating range (4.0–10.0), impressive environmental resistance for the co-existence of inorganic anions and mild toxic of photocatalytic intermediates demonstrated that the as-prepared BiU-*x* heterojunctions possessed good practical potential. Moreover, this research supplied a promising strategy to design and fabricate new p-n type MBCs for effectively eliminating pharmaceutical antibiotics.

Declaration of Competing Interest

The authors declare that they have no known competing financial interests or personal relationships that could have appeared to influence the work reported in this paper.

Data availability

Data will be made available on request.

Acknowledgments

This work was supported by National Natural Science Foundation of China (22176012, 51878023), Beijing Natural Science Foundation (8202016), Great Wall Scholars Training Program Project of Beijing Municipality Universities (CIT&TCD20180323), Beijing Talent Project (2020A27), Science and Technology General Project of Beijing Municipal Education Commission (KM202110016010), the Fundamental Research Funds for Beijing University of Civil Engineering and Architecture (X20147/X20141/X20135/X20146) and BUCEA Post Graduate Innovation Project (PG2021008).

Appendix A. Supplementary data

Supplementary data to this article can be found online at https://doi.org/10.1016/j.cej.2022.138624.

References

[1] X. Xiang, L. Wu, J. Zhu, J. Li, X. Liao, H. Huang, J. Fan, K. Lv, Photocatalytic degradation of sulfadiazine in suspensions of TiO_2 nanosheets with exposed (001) facets, Chin. Chem. Lett. 32 (2021) 3215–3220.
[2] D. Vione, B. Koehler, Modelled phototransformation kinetics of the antibiotic sulfadiazine in organic matter-rich lakes, Sci. Total Environ. 645 (2018) 1465–1473.
[3] W. Cai, Z. Zhou, X. Tan, W. Wang, W. Lv, H. Chen, Q. Zhao, Y.C.E.J. Yao, Magnetic iron phosphide particles mediated peroxymonosulfate activation for highly efficient elimination of sulfonamide antibiotics, Chem. Eng. J. 397 (2020), 125279.
[4] B. Wang, B.-J. Ni, Z. Yuan, J. Guo, Unravelling kinetic and microbial responses of enriched nitrifying sludge under long-term exposure of cephalexin and sulfadiazine, Water Res. 173 (2020), 115592.
[5] B. Li, T. Zhang, Biodegradation and adsorption of antibiotics in the activated sludge process, Environ. Sci. Technol. 44 (2010) 3468–3473.
[6] S. Tian, C. Zhang, D. Huang, R. Wang, G. Zeng, M. Yan, W. Xiong, C. Zhou, M. Cheng, W. Xue, Y. Yang, W. Wang, Recent progress in sustainable technologies for adsorptive and reactive removal of sulfonamides, Chem. Eng. J. 389 (2020), 123423.
[7] J. Hu, X. Li, F. Liu, W. Fu, L. Lin, B. Li, Comparison of chemical and biological degradation of sulfonamides: Solving the mystery of sulfonamide transformation, J. Hazard. Mater. 424 (2022), 127661.
[8] J. Yu, S. Zhu, L. Pang, P. Chen, G.-T. Zhu, Porphyrin-based magnetic nanocomposites for efficient extraction of polycyclic aromatic hydrocarbons from water samples, J. Chromatogr. A 1540 (2018) 1–10.
[9] J. Wang, S. Wang, Removal of pharmaceuticals and personal care products (PPCPs) from wastewater: A review, J. Environ. Manage. 182 (2016) 620–640.
[10] B.I. Escher, W. Pronk, M.J.F. Suter, M. Maurer, Monitoring the removal efficiency of pharmaceuticals and hormones in different treatment processes of source-separated urine with bioassays, Environ. Sci. Technol. 40 (2006) 5095–5101.
[11] Y. Xu, T. Liu, Y. Zhang, F. Ge, R.M. Steel, L. Sun, Advances in technologies for pharmaceuticals and personal care products removal, J. Mater. Chem. A 5 (2017) 12001–12014.
[12] A. Du, H. Fu, P. Wang, C. Zhao, C.-C. Wang, Enhanced catalytic peroxymonosulfate activation for sulfonamide antibiotics degradation over the supported CoS_x-CuS_x derived from ZIF-L(Co) immobilized on copper foam, J. Hazard. Mater. 426 (2022), 128134.
[13] F. Wang, H. Fu, F.-X. Wang, X.-W. Zhang, P. Wang, C. Zhao, C.-C. Wang, Enhanced catalytic sulfamethoxazole degradation via peroxymonosulfate activation over amorphous CoS_x@SiO_2 nanocages derived from ZIF-67, J. Hazard. Mater. 423 (2022), 126998.
[14] C.-C. Wang, J.-R. Li, X.-L. Lv, Y.-Q. Zhang, G. Guo, Photocatalytic organic pollutants degradation in metal–organic frameworks, Energy Environ. Sci. 7 (2014) 2831–2867.
[15] C.-C. Wang, X. Wang, W. Liu, The synthesis strategies and photocatalytic performances of TiO_2/MOFs composites: A state-of-the-art review, Chem. Eng. J. 391 (2020), 123601.
[16] C. Zhao, X. Pan, Z. Wang, C.-C. Wang, $1 + 1 > 2$: A critical review of MOF/bismuth-based semiconductor composites for boosted photocatalysis, Chem. Eng. J. 417 (2021), 128022.
[17] Z. Wang, M. Chen, D. Huang, G. Zeng, P. Xu, C. Zhou, C. Lai, H. Wang, M. Cheng, W. Wang, Multiply structural optimized strategies for bismuth oxyhalide photocatalysis and their environmental application, Chem. Eng. J. 374 (2019) 1025–1045.
[18] N. Tian, H. Huang, S. Wang, T. Zhang, X. Du, Y. Zhang, Facet-charge-induced coupling dependent interfacial photocharge separation: A case of BiOI/g-C_3N_4 pn junction, Appl. Catal. B 267 (2020), 118697.
[19] S. Ning, H. Lin, Y. Tong, X. Zhang, Q. Lin, Y. Zhang, J. Long, X. Wang, Dual couples Bi metal depositing and Ag@AgI islanding on BiOI 3D architectures for synergistic bactericidal mechanism of E. coli under visible light, Appl. Catal. B 204 (2017) 1–10.
[20] M. Sun, J. Hu, C. Zhai, M. Zhu, J.J.A.A.M. Pan, CuI as hole-transport channel for enhancing photoelectrocatalytic activity by constructing CuI/BiOI heterojunction, ACS Applied Materials, Interfaces 9 (2017) 13223–13230.
[21] Z. Liu, L. Wang, X. Yu, J. Zhang, R. Yang, X. Zhang, Y. Ji, M. Wu, L. Deng, L. Li, Piezoelectric-effect-enhanced full-spectrum photoelectrocatalysis in p-n heterojunction, Adv. Funct. Mater. 29 (2019) 1807279.
[22] H. Lu, Q. Hao, T. Chen, L. Zhang, D. Chen, C. Ma, W. Yao, Y. Zhu, A high-performance Bi_2O_3/Bi_2SiO_5 p-n heterojunction photocatalyst induced by phase transition of Bi_2O_3, Appl. Catal. B 237 (2018) 59–67.
[23] P.J. Mafa, B.B. Mamba, A.T. Kuvarega, Construction of hierarchical $BiPW_{12}O_{40}$/BiOI p–n heterojunction with enhanced visible light activity for degradation of endocrine disrupting Bisphenol A, Sep. Purif. Technol. 253 (2020), 117349.
[24] Y. Liu, W. Yao, D. Liu, R. Zong, M. Zhang, X. Ma, Y. Zhu, Enhancement of visible light mineralization ability and photocatalytic activity of $BiPO_4$/BiOI, Appl. Catal. B 163 (2015) 547–553.
[25] C. Zhang, W. Fei, H. Wang, N. Li, D. Chen, Q. Xu, H. Li, J. He, J. Lu, pn Heterojunction of BiOI/ZnO nanorod arrays for piezo-photocatalytic degradation of bisphenol A in water, J. Hazard. Mater. 399 (2020), 123109.
[26] J. Zhang, J. Fu, Z. Wang, B. Cheng, K. Dai, W. Ho, Direct Z-scheme porous g-C_3N_4/BiOI heterojunction for enhanced visible-light photocatalytic activity, J. Alloys Compd. 766 (2018) 841–850.
[27] C.-C. Wang, J.-R. Li, X.-L. Lv, Y.-Q. Zhang, G. Guo, Photocatalytic organic pollutants degradation in metal–organic frameworks, Energy Environ. Sci. 7 (2014) 2831–2867.
[28] C.-Y. Wang, L. Ma, C.-C. Wang, P. Wang, L. Gutierrez, W. Zheng, Light-response adsorption and desorption behaviors of metal–organic frameworks, Environ. Funct. Mater. (2022), https://doi.org/10.1016/j.efmat.2022.05.002.
[29] M. Kandiah, M.H. Nilsen, S. Usseglio, S. Jakobsen, U. Olsbye, M. Tilset, C. Larabi, E.A. Quadrelli, F. Bonino, K.P. Lillerud, Synthesis and stability of tagged UiO-66 Zr-MOFs, Chem. Mater. 22 (2010) 6632–6640.
[30] Z. Man, Y. Meng, X. Lin, X. Dai, L. Wang, D. Liu, Assembling UiO-66@TiO_2 nanocomposites for efficient photocatalytic degradation of dimethyl sulfide, Chem. Eng. J. 431 (2022), 133952.
[31] R. Bariki, D. Majhi, K. Das, A. Behera, B. Mishra, Facile synthesis and photocatalytic efficacy of UiO-66/$CdIn_2S_4$ nanocomposites with flowerlike 3D-microspheres towards aqueous phase decontamination of triclosan and H_2 evolution, Appl. Catal. B 270 (2020), 118882.
[32] C. Zhao, Z. Wang, X. Li, X. Yi, H. Chu, X. Chen, C.-C. Wang, Facile fabrication of BUC-21/$Bi_{24}O_{31}Br_{10}$ composites for enhanced photocatalytic Cr (VI) reduction under white light, Chem. Eng. J. 389 (2020), 123431.
[33] C. Sirtori, A. Zapata, I. Oller, W. Gernjak, A. Aguera, S. Malato, Decontamination industrial pharmaceutical wastewater by combining solar photo-Fenton and biological treatment, Water Res. 43 (2009) 661–668.
[34] M.M. Ahmed, S. Barbati, P. Doumenq, S. Chiron, Sulfate radical anion oxidation of diclofenac and sulfamethoxazole for water decontamination, Chem. Eng. J. 197 (2012) 440–447.
[35] C. Sahoo, A. Gupta, Optimization of photocatalytic degradation of methyl blue using silver ion doped titanium dioxide by combination of experimental design and response surface approach, J. Hazard. Mater. 215 (2012) 302–310.
[36] W. Yang, R.G. Parr, R. Pucci, Electron density, Kohn-Sham frontier orbitals, and Fukui functions, J. Chem. Phys. 81 (1984) 2862–2863.
[37] S. Li, T. Huang, P. Du, W. Liu, J. Hu, Photocatalytic transformation fate and toxicity of ciprofloxacin related to dissociation species: Experimental and theoretical evidences, Water Res. 185 (2020), 116286.
[38] K.B. Wiberg, M. Frisch, Effect of conjugation on electron distributions separation of σ and π terms, J. Chem. Theory Comput. 12 (2016) 1220–1227.
[39] X.-H. Yi, S.-Q. Ma, X.-D. Du, C. Zhao, H. Fu, P. Wang, C.-C. Wang, The facile fabrication of 2D/3D Z-scheme g-C_3N_4/UiO-66 heterojunction with enhanced photocatalytic Cr (VI) reduction performance under white light, Chem. Eng. J. 375 (2019), 121944.
[40] Y.-H. Li, X.-H. Yi, Y.-X. Li, C.-C. Wang, P. Wang, C. Zhao, W. Zheng, Robust Cr (VI) reduction over hydroxyl modified UiO-66 photocatalyst constructed from mixed ligands: Performances and mechanism insight with or without tartaric acid, Environ. Res. 201 (2021), 111596.
[41] Y. Fu, K. Zhang, Y. Zhang, Y. Cong, Q. Wang, Fabrication of visible-light-active MR/NH_2-MIL-125 (Ti) homojunction with boosted photocatalytic performance, Chem. Eng. J. 412 (2021), 128722.
[42] J. Ding, Z. Yang, C. He, X. Tong, Y. Li, X. Niu, H. Zhang, UiO-66 (Zr) coupled with Bi_2MoO_6 as photocatalyst for visible-light promoted dye degradation, Journal of Colloid, Interface Sci. 497 (2017) 126–133.
[43] C. Chang, L. Zhu, S. Wang, X. Chu, L. Yue, Novel mesoporous graphite carbon nitride/BiOI heterojunction for enhancing photocatalytic performance under visible-light irradiation, ACS Appl. Mater. Interfaces 6 (2014) 5083–5093.
[44] X.-Y. Xu, C. Chu, H. Fu, X.-D. Du, P. Wang, W. Zheng, C.-C. Wang, Light-responsive UiO-66-NH_2/Ag_3PO_4 MOF-nanoparticle composites for the capture and release of sulfamethoxazole, Chem. Eng. J. 350 (2018) 436–444.
[45] K.-Y.-A. Lin, S.-Y. Chen, A.P. Jochems, Zirconium-based metal organic frameworks: Highly selective adsorbents for removal of phosphate from water and urine, Mater. Chem. Phys. 160 (2015) 168–176.

[46] Q. Hu, Y. Chen, M. Li, Y. Zhang, B. Wang, Y. Zhao, J. Xia, S. Yin, H. Li, Construction of NH_2-UiO-66/BiOBr composites with boosted photocatalytic activity for the removal of contaminants, Colloids Surf. A Physicochem. Eng. Aspects 579 (2019), 123625.

[47] J. Yang, Y. Dai, X. Zhu, Z. Wang, Y. Li, Q. Zhuang, J. Shi, J. Gu, Metal-organic frameworks with inherent recognition sites for selective phosphate sensing through their coordination-induced fluorescence enhancement effect, J. Mater. Chem. A 3 (2015) 7445–7452.

[48] J. Wang, C. Cao, Y. Wang, Y. Wang, B. Sun, L. Zhu, In situ preparation of pn BiOI@Bi_5O_7I heterojunction for enhanced PFOA photocatalytic degradation under simulated solar light irradiation, Chem. Eng. J. 391 (2020), 123530.

[49] X.-J. Wen, C.-G. Niu, L. Zhang, G.-M. Zeng, Novel p-n heterojunction BiOI/CeO_2 photocatalyst for wider spectrum visible-light photocatalytic degradation of refractory pollutants, Dalton Trans. 46 (2017) 4982–4993.

[50] Y. Park, Y. Na, D. Pradhan, B.-K. Min, Y. Sohn, Adsorption and UV/Visible photocatalytic performance of BiOI for methyl orange, Rhodamine B and methylene blue: Ag and Ti-loading effects, CrystEngComm 16 (2014) 3155–3167.

[51] X. Shi, P. Wang, W. Li, Y. Bai, H. Xie, Y. Zhou, L. Ye, Change in photocatalytic NO removal mechanisms of ultrathin BiOBr/BiOI via NO_3^- adsorption, Appl. Catal. B 243 (2019) 322–329.

[52] H. Fu, S. Ma, P. Zhao, S. Xu, S. Zhan, Activation of peroxymonosulfate by graphitized hierarchical porous biochar and $MnFe_2O_4$ magnetic nanoarchitecture for organic pollutants degradation: Structure dependence and mechanism, Chem. Eng. J. 360 (2019) 157–170.

[53] R. Hao, G. Wang, H. Tang, L. Sun, C. Xu, D. Han, Template-free preparation of macro/mesoporous g-C_3N_4/TiO_2 heterojunction photocatalysts with enhanced visible light photocatalytic activity, Appl. Catal. B 187 (2016) 47–58.

[54] Q. Huang, C. Wang, D. Hao, W. Wei, L. Wang, B.-J. Ni, Ultralight biodegradable 3D-g-C_3N_4 aerogel for advanced oxidation water treatment driven by oxygen delivery channels and triphase interfaces, J. Cleaner Prod. 288 (2021), 125091.

[55] Y.C. Zhang, Z.N. Du, K.W. Li, M. Zhang, D.D. Dionysiou, High-performance visible-light-driven SnS_2/SnO_2 nanocomposite photocatalyst prepared via in situ hydrothermal oxidation of SnS_2 nanoparticles, ACS Appl. Mater. Interfaces 3 (2011) 1528–1537.

[56] X. Mu, J. Jiang, F. Chao, Y. Lou, J. Chen, Ligand modification of UiO-66 with an unusual visible light photocatalytic behavior for RhB degradation, Dalton Trans. 47 (2018) 1895–1902.

[57] T.B. Li, G. Chen, C. Zhou, Z.Y. Shen, R.C. Jin, J.X. Sun, New photocatalyst BiOCl/BiOI composites with highly enhanced visible light photocatalytic performances, Dalton Trans. 40 (2011) 6751–6758.

[58] W. Xia, C. Jin, S. Kundu, M. Muhler, A highly efficient gas-phase route for the oxygen functionalization of carbon nanotubes based on nitric acid vapor, Carbon 47 (2009) 919–922.

[59] B. Thierry, J. Ng, T. Krieg, H.J. Griesser, A robust procedure for the functionalization of gold nanorods and noble metal nanoparticles, Chem. Commun. (2009) 1724–1726.

[60] K. Zhang, K.C. Kemp, V. Chandra, Homogeneous anchoring of TiO_2 nanoparticles on graphene sheets for waste water treatment, Mater. Lett. 81 (2012) 127–130.

[61] Y. Naciri, A. Bouddouch, B. Bakiz, A. Taoufyq, M. Ezahri, A. Benlhachemi, Photocatalytic degradation of sulfadiazine by $Zn_3(PO_4)_2$/$BiPO_4$ composites upon UV light irradiation, Mater. Today:. Proc. 22 (2020) 48–51.

[62] A. Singh, S. Karmakar, S. Basu, Role of sputtered WO_3 underlayer and NiFeCr-LDH co-catalyst in WO_3-$BiVO_4$ heterojunction for enhanced photoelectrochemical water oxidation, Int. J. Hydrogen Energy 46 (2021) 39868–39881.

[63] Y. Bai, L. Ye, T. Chen, L. Wang, X. Shi, X. Zhang, D. Chen, Facet-dependent photocatalytic N_2 fixation of bismuth-rich Bi_5O_7I nanosheets, ACS Appl. Mater. Interfaces 8 (2016) 27661–27668.

[64] Y.-X. Li, C.-C. Wang, H. Fu, P. Wang, Marigold-flower-like TiO_2/MIL-125 core-shell composite for enhanced photocatalytic Cr (VI) reduction, J. Environ. Chem. Eng. 9 (2021), 105451.

[65] C. Zhao, S.-J. Gao, L. Zhou, X. Li, X. Chen, C.-C. Wang, Dissolved organic matter in urban forestland soil and its interactions with typical heavy metals: a case of Daxing District, Beijing, Environ. Sci. Pollut. Res. 26 (2019) 2960–2973.

[66] L. Cheng, Y. Kang, Selective preparation of Bi_2O_3 visible light-driven photocatalyst by dispersant and calcination, J. Alloys Compd. 585 (2014) 85–93.

[67] Z. Hu, X. Xie, S. Li, M. Song, G. Liang, J. Zhao, Z. Wang, Rational construct CQDs/BiOCOOH/uCN photocatalyst with excellent photocatalytic performance for degradation of sulfathiazole, Chem. Eng. J. 404 (2021), 126541.

[68] Y. Duan, S. Zhou, L. Deng, Z. Shi, H. Jiang, S. Zhou, Enhanced photocatalytic degradation of sulfadiazine via g-C_3N_4/carbon dots nanosheets under nanoconfinement: synthesis biocompatibility and mechanism, J. Environ. Chem. Eng. 8 (2020), 104612.

[69] M. Liu, D. Zhang, J. Han, C. Liu, Y. Ding, Z. Wang, A. Wang, Adsorption enhanced photocatalytic degradation sulfadiazine antibiotic using porous carbon nitride nanosheets with carbon vacancies, Chem. Eng. J. 382 (2020), 123017.

[70] P. Dhiman, N. Dhiman, A. Kumar, G. Sharma, M. Naushad, A.A. Ghfar, Solar active nano-$Zn_{1-x}Mg_xFe_2O_4$ as a magnetically separable sustainable photocatalyst for degradation of sulfadiazine antibiotic, J. Mol. Liq. 294 (2019), 111574.

[71] C.-X. Chen, S.-S. Yang, J. Ding, G.-Y. Wang, L. Zhong, S.-Y. Zhao, Y.-N. Zang, J.-Q. Jiang, L. Ding, Y. Zhao, Non-covalent self-assembly synthesis of AQ2S@rGO nanocomposite for the degradation of sulfadiazine under solar irradiation: The indispensable effect of chloride, Appl. Catal. B 298 (2021), 120495.

[72] Z. Guan, Q. Li, B. Shen, S. Bao, J. Zhang, B. Tian, Fabrication of Co_3O_4 and Au co-modified BiOBr flower-like microspheres with high photocatalytic efficiency for sulfadiazine degradation, Sep. Purif. Technol. 234 (2020), 116100.

[73] Q. Dong, F. Yang, F. Liang, Y. Zhang, D. Xia, W. Zhao, L. Wu, X. Liu, Z. Jiang, C. Sun, Silver particle on $BiVO_4$ nanosheet plasmonic photocatalyst with enhanced photocatalytic oxidation activity of sulfadiazine, J. Mol. Liq. 331 (2021), 115751.

[74] J. Li, L. Meng, F. Wang, M. Han, Y. Guo, Z. Wei, X. Shi, C. Sun, Room temperature aqueous synthesis of $BiVO_4$/$NaBiO_3$ heterojunction with high efficiency for sulfadiazine removal, Catal. Commun. 86 (2016) 51–54.

[75] D. Li, N. Zhang, R. Yuan, H. Chen, F. Wang, B. Zhou, Effect of wavelengths on photocatalytic oxidation mechanism of sulfadiazine and sulfamethoxazole in the presence of TiO_2, J. Environ. Chem. Eng. 9 (2021), 106243.

[76] X. Xie, Y. Liu, X. Dong, C. Lin, X. Wen, Q. Yan, Synthesis and characterization of Fe_3O_4/BiOI np heterojunction magnetic photocatalysts, Appl. Surf. Sci. 455 (2018) 742–747.

[77] R. Zhang, M. Chen, Z. Xiong, Y. Guo, B. Lai, Highly efficient degradation of emerging contaminants by magnetic CuO@Fe_xO_y derived from natural mackinawite (FeS) in the presence of peroxymonosulfate, Chin. Chem. Lett. 33 (2022) 948–952.

[78] P. Yang, Y. Ye, Z. Yan, Q. Li, K. Zhang, Y. Yang, Q. Zhang, H. Yin, D. Xia, F. Pan, Efficient removal of tetracycline in water by a novel chemical and biological coupled system with non-woven cotton fabric as carrier, Chin. Chem. Lett. 32 (2021) 2823–2827.

[79] X. Xu, L. Meng, J. Luo, M. Zhang, Y. Wang, Y. Dai, C. Sun, Z. Wang, S. Yang, H. He, Self-assembled ultrathin CoO/Bi quantum dots/defective Bi_2MoO_6 hollow Z-scheme heterojunction for visible light-driven degradation of diazinon in water matrix: Intermediate toxicity and photocatalytic mechanism, Appl. Catal. B 293 (2021), 120231.

[80] P. Gholami, A. Khataee, B. Vahid, A. Karimi, M. Golizadeh, M. Ritala, Sonophotocatalytic degradation of sulfadiazine by integration of microfibrillated carboxymethyl cellulose with Zn-Cu-Mg mixed metal hydroxide/g-C_3N_4 composite, Sep. Purif. Technol. 245 (2020), 116866.

[81] X. Liu, Y. Liu, S. Lu, W. Guo, B. Xi, Performance and mechanism into TiO_2/Zeolite composites for sulfadiazine adsorption and photodegradation, Chem. Eng. J. 350 (2018) 131–147.

[82] F. Ghribi, M. Sehailia, L. Aoudjit, F. Touahra, D. Zioui, A. Boumechhour, D. Halliche, K. Bachari, Z. Benmaamar, Solar-light promoted photodegradation of metronidazole over ZnO-$ZnAl_2O_4$ heterojunction derived from 2D-layered double hydroxide structure, J. Photochem. Photobiol. A Chem. 397 (2020), 112510.

[83] Y. Song, J. Tian, S. Gao, P. Shao, J. Qi, F. Cui, Photodegradation of sulfonamides by g-C_3N_4 under visible light irradiation: effectiveness, mechanism and pathways, Appl. Catal. B 210 (2017) 88–96.

[84] U.G. Akpan, B.H. Hameed, Parameters affecting the photocatalytic degradation of dyes using TiO_2-based photocatalysts: a review, J. Hazard. Mater. 170 (2009) 520–529.

[85] W. Shi, Y. Yan, X. Yan, Microwave-assisted synthesis of nano-scale $BiVO_4$ photocatalysts and their excellent visible-light-driven photocatalytic activity for the degradation of ciprofloxacin, Chem. Eng. J. 215 (2013) 740–746.

[86] J. Wiszniowski, D. Robert, J. Surmacz-Gorska, K. Miksch, S. Malato, J.-V. Weber, Solar photocatalytic degradation of humic acids as a model of organic compounds of landfill leachate in pilot-plant experiments: influence of inorganic salts, Appl. Catal. B 53 (2004) 127–137.

[87] F. Chen, Q. Yang, Y. Zhong, H. An, J. Zhao, T. Xie, Q. Xu, X. Li, D. Wang, G. Zeng, Photo-reduction of bromate in drinking water by metallic Ag and reduced graphene oxide (RGO) jointly modified $BiVO_4$ under visible light irradiation, Water Res. 101 (2016) 555–563.

[88] S. Huang, C. Chen, H. Tsai, J. Shaya, C. Lu, Photocatalytic degradation of thiobencarb by a visible light-driven MoS_2 photocatalyst, Sep. Purif. Technol. 197 (2018) 147–155.

[89] J. Brame, M. Long, Q. Li, P. Alvarez, Inhibitory effect of natural organic matter or other background constituents on photocatalytic advanced oxidation processes: Mechanistic model development and validation, Water Res. 84 (2015) 362–371.

[90] C.S. Uyguner-Demirel, M. Bekbolet, Significance of analytical parameters for the understanding of natural organic matter in relation to photocatalytic oxidation, Chemosphere 84 (2011) 1009–1031.

[91] X. Yang, F.L. Rosario-Ortiz, Y. Lei, Y. Pan, X. Lei, P. Westerhoff, Multiple Roles of Dissolved Organic Matter in Advanced Oxidation Processes, Environ. Sci. Technol. (2022), https://doi.org/10.1021/acs.est.2c01017.

[92] X. Ao, Z. Li, H. Zhang, A comprehensive insight into a rapid degradation of sulfamethoxazole by peroxymonosulfate enhanced UV-A LED/g-C_3N_4 photocatalysis, J. Cleaner Prod. 356 (2022), 131822.

[93] T. Lan, J. Liao, Y. Yang, Z. Chai, N. Liu, D. Wang, Competition/cooperation between humic acid and graphene oxide in uranyl adsorption implicated by molecular dynamics simulations, Environ. Sci. Technol. 53 (2019) 5102–5110.

[94] D.D. Chen, X.H. Yi, L. Ling, C.C. Wang, P. Wang, Photocatalytic Cr (VI) sequestration and photo-Fenton bisphenol A decomposition over white light responsive PANI/MIL-88A (Fe), Appl. Organomet. Chem. 34 (2020) e5795.

[95] C. Zhao, J. Wang, X. Chen, Z. Wang, H. Ji, L. Chen, W. Liu, C.-C. Wang, Bifunctional $Bi_{12}O_{17}Cl_2$/MIL-100 (Fe) composites toward photocatalytic Cr (VI) sequestration and activation of persulfate for bisphenol A degradation, Sci. Total Environ. 752 (2021), 141901.

[96] X. Wei, P. Wang, H. Fu, C. Zhao, C.-C. Wang, Boosted photocatalytic elimination toward Cr (VI) and organic pollutants over BUC-21/$Cd_{0.5}Zn_{0.5}S$ under LED visible Light, Mater. Res. Bull. 129 (2020), 110903.

[97] Q. Hao, R. Wang, H. Lu, W. Ao, D. Chen, C. Ma, W. Yao, Y. Zhu, One-pot synthesis of C/Bi/Bi_2O_3 composite with enhanced photocatalytic activity, Appl. Catal. B 219 (2017) 63–72.

[98] H. Yu, J. Huang, L. Jiang, L. Leng, K. Yi, W. Zhang, C. Zhang, X. Yuan, In situ construction of Sn-doped structurally compatible heterojunction with enhanced interfacial electric field for photocatalytic pollutants removal and CO_2 reduction, Appl. Catal. B 298 (2021), 120618.
[99] Z. Chen, C. Lian, K. Huang, J. Ji, Q. Yan, J. Zhang, M. Xing, "Small amount for multiple times" of H_2O_2 feeding way in MoS_2-Fe_x heterogeneous fenton for enhancing sulfadiazine degradation, Chin. Chem. Lett. 33 (2022) 1365–1372.
[100] Y. Chen, S. Lan, M. Zhu, Construction of piezoelectric $BaTiO_3$/MoS_2 heterojunction for boosting piezo-activation of peroxymonosulfate, Chin. Chem. Lett. 32 (2021) 2052–2056.
[101] Y. Jiang, Z. Xiong, J. Huang, F. Yan, G. Yao, B. Lai, Effective E. coli inactivation of core-shell ZnO@ZIF-8 photocatalysis under visible light synergize with peroxymonosulfate: Efficiency and mechanism, Chin. Chem. Lett. 33 (2022) 415–423.
[102] H. Winnischofer, A.L.B. Formiga, M. Nakamura, H.E. Toma, K. Araki, A. F. Nogueira, Conduction and photoelectrochemical properties of monomeric and electropolymerized tetraruthenated porphyrin films, Photochem. Photobiol. Sci. 4 (2005) 359–366.
[103] D.P. Kumar, E.H. Kim, H. Park, S.Y. Chun, M. Gopannagari, P. Bhavani, D. A. Reddy, J.K. Song, T.K. Kim, Tuning band alignments and charge-transport properties through $MoSe_2$ bridging between MoS_2 and cadmium sulfide for enhanced hydrogen production, ACS Appl. Mater. Interfaces 10 (2018) 26153–26161.
[104] Q. Xue, Z. Wang, S. Han, Y. Liu, X. Dou, Y. Li, H. Zhu, X. Yuan, Ligands engineering of Au nanoclusters with multifunctional metalloporphyrin for photocatalytic H_2O_2 production, J. Mater. Chem. A 15 (2022) 8371–8377.
[105] H. Gong, Z. Li, Z. Chen, Q. Liu, M. Song, C. Huang, NiSe/$Cd_{0.5}Zn_{0.5}S$ composite nanoparticles for use in p–n heterojunction-based photocatalysts for solar energy harvesting, ACS Appl. Nano Mater. 3 (2020) 3665–3674.
[106] M. Chen, C. Guo, S. Hou, J. Lv, Y. Zhang, H. Zhang, J. Xu, A novel Z-scheme AgBr/Pg-C_3N_4 heterojunction photocatalyst: excellent photocatalytic performance and photocatalytic mechanism for ephedrine degradation, Appl. Catal. B 266 (2020), 118614.
[107] S. Li, C. Wang, Y. Liu, M. Cai, Y. Wang, H. Zhang, Y. Guo, W. Zhao, Z. Wang, X. Chen, Photocatalytic degradation of tetracycline antibiotic by a novel $Bi_2Sn_2O_7$/Bi_2MoO_6 S-scheme heterojunction: Performance, mechanism insight and toxicity assessment, Chem. Eng. J. 429 (2022), 132519.
[108] J. Monteagudo, A. Durán, M. Martínez, I. San Martín, Effect of reduced graphene oxide load into TiO_2 P25 on the generation of reactive oxygen species in a solar photocatalytic reactor. Application to antipyrine degradation, Chem. Eng. J. 380 (2020), 122410.
[109] F. Dong, C. Li, J. Crittenden, T. Zhang, Q. Lin, G. He, W. Zhang, J. Luo, Sulfadiazine destruction by chlorination in a pilot-scale water distribution system: kinetics, pathway, and bacterial community structure, J. Hazard. Mater. 366 (2019) 88–97.
[110] J. Gao, C. Hedman, C. Liu, T. Guo, J.A. Pedersen, Transformation of sulfamethazine by manganese oxide in aqueous solution, Environ. Sci. Technol. 46 (2012) 2642–2651.
[111] L. Chen, H. Ji, J. Qi, T. Huang, C.-C. Wang, W. Liu, Degradation of acetaminophen by activated peroxymonosulfate using $Co(OH)_2$ hollow microsphere supported titanate nanotubes: Insights into sulfate radical production pathway through CoOH activation, Chem. Eng. J. 406 (2021), 126877.